REDUCTION OF LAYER 5 MEDIATED LONG-RANGE CORTICAL COMMUNICATION BY ANTIPSYCHOTIC DRUGS

Matthias Heindorf[1] & Georg B. Keller[1,2,3]

[1]Friedrich Miescher Institute for Biomedical Research, Basel, Switzerland
[2]Faculty of Natural Sciences, University of Basel, Basel, Switzerland
[3]To whom correspondence should be addressed.

Psychosis is characterized by a diminished ability of the brain to distinguish externally driven activity patterns from self-generated activity patterns. Antipsychotic drugs are a class of small molecules with relatively broad binding affinity for a variety of neuromodulator receptors that, in humans, can prevent or ameliorate psychosis. How these drugs influence the function of cortical circuits and in particular their ability to identify self-generated activity patterns is still largely unclear. Here we used widefield calcium imaging to determine the cell type specific functional effects of antipsychotic drugs in mouse dorsal cortex during visuomotor integration. By comparing cell type specific activation patterns between locomotion onsets that were experimentally coupled to self-generated visual feedback and locomotion onsets that were not coupled, we show that deep cortical layers were differentially activated in these two conditions. We then show that the antipsychotic drug clozapine disrupted visuomotor integration at locomotion onsets also primarily in deep cortical layers. Given that one of the key components of visuomotor integration in cortex are long-range cortico-cortical connections, we tested whether the effect of clozapine was detectable in the correlation structure of activity patterns across dorsal cortex. We found that clozapine, as well as two other antipsychotic drugs, aripiprazole and haloperidol, resulted in a strong reduction in correlations of layer 5 activity between cortical areas and impaired the spread of visuomotor prediction errors generated in visual cortex. Our results are consistent with the interpretation that a major functional effect of antipsychotic drugs is an alteration of the activation of internal representations as a consequence of reduced long-range layer 5 mediated communication.

**** Dear reader, please note this manuscript is formatted in a standard submission format, and all statistical information is provided in Table S1. ****

INTRODUCTION

Under normal conditions, self-generated movements are coupled to sensory feedback in different modalities. Locomotion, for example, is coupled to proprioceptive feedback from muscle

33 movements, somatosensory and auditory feedback from touching the ground, vestibular feedback
34 from translational acceleration, and visual feedback in the form of expanding visual flow. This
35 coupling is key to our brain's ability to learn internal models of the world (Jordan and Rumelhart,
36 1992). Internal models are the transformations between cortical areas and can be used to predict
37 the sensory consequences of movement. Hallucinations and delusions can be explained as a
38 misconfiguration of these internal models: assuming the predictions of the sensory consequences of
39 movements are inaccurate this can result in self-generated activity that is not correctly distinguished
40 from externally driven activity (Fletcher and Frith, 2009; Frith, 2005).

41 Self-generated movements result in broad activation of most regions of the brain (Musall et al.,
42 2019; Stringer et al., 2019), including some primary sensory areas like visual cortex (Keller et al.,
43 2012; Saleem et al., 2013) where they have been shown to depend on visual context (Pakan et al.,
44 2016). The framework of predictive processing postulates that in cortex, these movement related
45 signals are internal model based predictions of the sensory consequences of movement that are
46 compared to externally generated bottom-up input to compute prediction errors (Jiang and Rao,
47 2021; Keller and Mrsic-Flogel, 2018). Evidence for this interpretation has mainly come from the
48 discovery of movement related prediction error responses in a variety of different cortical regions
49 and species (Attinger et al., 2017; Audette et al., 2021; Ayaz et al., 2019; Eliades and Wang, 2008;
50 Heindorf et al., 2018; Keller and Hahnloser, 2009; Keller et al., 2012; Stanley and Miall, 2007; Zmarz
51 and Keller, 2016), and the observation that top-down inputs from motor areas of cortex appear to
52 carry movement related predictions of sensory input to sensory areas of cortex (Audette et al., 2021;
53 Leinweber et al., 2017). The neurons on which the opposing bottom-up input and top-down
54 prediction converge are referred to as prediction error neurons and are thought to reside primarily
55 in layer 2/3 of cortex (Jordan and Keller, 2020). To complete the circuit there then needs to be a
56 population of neurons that integrate over prediction error responses. These are referred to as
57 internal representation neurons. It is still unclear which cortical neuron type might function as
58 internal representation neurons but based on anatomical arguments it is often speculated that they
59 can be found in deep cortical layers (Bastos et al., 2012).

60 In humans, externally driven and self-generated activity patterns can be experimentally separated at
61 least partially, for example, by showing subjects a visual stimulus and then later asking them to
62 visualize the same stimulus (Le Bihan et al., 1993). This type of experiment is considerably more
63 difficult to perform in animals. Using movement as a proxy for self-generated activity patterns,
64 however, we can compare a condition in which self-generated and externally generated activity
65 patterns are correlated to a condition in which they are not. In the visual system, we can use a

virtual reality environment to experimentally couple or decouple locomotion from visual flow feedback. We will refer to the former as a closed loop condition and to the latter as an open loop condition. Assuming the predictive processing model is correct, we should find differences in activation patterns in dorsal cortex in responses to locomotion onsets as a function of whether they occurred with or without coupled visual flow feedback. Both prediction error neurons as well as internal representation neurons should respond differentially. Thus, we set out to investigate whether there are differences between closed and open loop activation patterns of mouse dorsal cortex, and whether these differences are neuron type specific. Then, if hallucinations are indeed the result of aberrant activation of internal representations, possibly as a result of misconfigured internal models, antipsychotic drugs should alter differential activation patterns.

RESULTS

Tlx3 positive layer 5 (L5) intratelencephalic (IT) neurons distinguished closed and open loop visuomotor coupling

To investigate neuron type specific differences in activity patterns at locomotion onsets with and without self-generated visual feedback in mouse dorsal cortex, we quantified locomotion onset activity using widefield calcium imaging (Wekselblatt et al., 2016). A GCaMP variant was expressed using either a retroorbital injection of an AAV-PHP.eB vector (Chan et al., 2017), or a cross between a Cre line and the Ai148 GCaMP6 reporter line (Daigle et al., 2018) (see Methods; **Figure 1A**, **Table S2**). Mice either expressed a GCaMP variant either brain wide (C57BL/6), or in genetically identified subsets of excitatory or inhibitory neurons using Cre driver lines. Please note, we use the term 'brain wide' here to describe an expression pattern that was determined by the combination of the AAV-PHP.eB tropism intersected with the expression pattern of EF1α or hSyn1 promoters but that was otherwise brain wide (see Discussion). We used Emx1-Cre mice to target expression to cortical excitatory neurons (Gorski et al., 2002), Cux2-CreERT2 mice to target expression predominantly to layer 2/3 but also layer 4 excitatory neurons (Franco et al., 2012), Scnn1a-Cre mice to target expression to a subset of layer 4 excitatory neurons (Madisen et al., 2010), Tlx3-Cre mice to target expression to a subset of layer 5 IT neurons (Gerfen et al., 2013), and Ntsr1-Cre mice to target expression to a subset of layer 6 excitatory neurons (Gong et al., 2007). To target subpopulations of inhibitory neurons, we used PV-Cre (Hippenmeyer et al., 2005), VIP-Cre (Taniguchi et al., 2011), and SST-Cre mice (Taniguchi et al., 2011) (see Methods). Prior to the start of the imaging experiments, mice were implanted with a crystal skull cranial window (Kim et al., 2016). We used crystal skull preparations as we found that hemodynamic artifacts were smaller in this preparation compared to those observed in clear skull preparations (**Figure S1**). For all experiments, mice were head fixed and

free to locomote on a spherical treadmill (**Figure 1B**). Activity from dorsal cortex was imaged while mice were in a closed loop visuomotor condition, in which locomotion on the spherical treadmill controlled forward movement in a virtual corridor. Following this, mice were exposed to an open loop condition during which mice were presented with a replay of the visual flow they had self-generated in the preceding closed loop condition.

We first compared locomotion onset responses in the closed loop condition to those in the open loop condition in mice that expressed GCaMP brain wide (C57BL/6). Consistent with previous findings (Musall et al., 2019; Stringer et al., 2019), we found that locomotion onset resulted in broad activation across most of dorsal cortex in both the closed and open loop conditions (**Figure 1C**). However, comparing the same locomotion onsets in mice that expressed GCaMP6 only in Tlx3 positive L5 IT neurons, we found that the activation pattern at locomotion onset was strikingly different between closed and open loop conditions (**Figure 1D**). While locomotion onset in the open loop condition resulted in an increase in activity across dorsal cortex similar to that observed in the C57BL/6 mice with brain wide GCaMP expression, locomotion onset in the closed loop condition resulted in a very different activation pattern: In posterior parts of dorsal cortex, activity decreased, while in frontal parts of the dorsal cortex, activity increased. To quantify these activation patterns across mice, we selected six regions of interest: primary visual cortex (V1), antero-medial secondary visual cortex (V2am), retrosplenial cortex (RSC), primary motor cortex (M1), the anterior cingulate cortex at the level of bregma (A24b), and secondary motor cortex (M2) (**Figure 1E**). In C57BL/6 mice that expressed GCaMP brain wide, closed loop locomotion onset resulted in similar activity patterns across these six regions (**Figure 1F**). This activity pattern was not markedly different from that observed during locomotion onsets in an open loop condition (**Figure 1G**). To quantify the contribution of visual flow onset to the closed loop locomotion onset activity, we measured responses to visual flow onsets that occurred in the absence of locomotion in the open loop condition (**Figure 1H**). In C57BL/6 mice with brain wide GCaMP expression, visual flow onsets resulted in responses that were small compared to those observed during locomotion onset, even in V1. Note that a visual flow onset is a relatively weak visual stimulus compared to a drifting grating stimulus. A grating stimulus is typically composed of a gray screen or a standing grating stimulus that suddenly transitions to a drifting grating, and thus the visual flow undergoes a very high acceleration. A visual flow onset in an open loop condition is the replay of previously self-generated visual flow and thus exhibits much lower visual flow acceleration. The absence of a strong visual flow onset response in C57BL/6 mice that expressed GCaMP brain wide is consistent with a high similarity of closed and open loop locomotion onset responses.

In mice that expressed GCaMP6 in Tlx3 positive L5 IT neurons, the closed loop locomotion onset patterns differed markedly when compared across the six regions of interest (**Figure 1I**). Moreover, these activation patterns were different from those observed during open loop locomotion onsets (**Figure 1J**). In Tlx3 positive L5 IT neurons, open loop visual flow onsets that occurred in the absence of locomotion resulted in quantifiable responses in V1 and V2am (**Figure 1K**), but the closed loop locomotion onset responses could not be explained by the sum of locomotion and visual flow onset responses (**Figure S2**). We repeated these experiments and analyses for the other excitatory and inhibitory cortical neuron types (**Figure S3**). For each neuron type, we quantified the similarity of the activity patterns associated with closed and open loop locomotion onsets by calculating the correlation coefficient between the activity traces in a window around locomotion onset (-5 s to +3 s) and averaging across regions of interest (see Methods). We found the highest similarity between closed and open loop locomotion onsets in C57BL/6 mice that expressed GCaMP brain wide and in mice that expressed GCaMP6 in PV positive interneurons, and the similarity was lowest in mice that expressed GCaMP6 in Tlx3 positive L5 IT and Ntsr1 positive layer 6 excitatory neurons (**Figures 1L**). Thus, excitatory neurons of deep cortical layers exhibited the strongest differences between closed and open loop locomotion related activation. The remarkable aspect of these findings is not that there are differences between closed and open loop locomotion onsets, particularly in visual regions of cortex one would perhaps expect to find differences, but that these differences are larger specifically in the deep cortical layers.

To quantify how the interaction between locomotion and visual flow feedback changes across dorsal cortex, we computed correlations between calcium activity and locomotion speed for each region of interest, for closed and open loop conditions separately. In C57BL/6 mice that expressed GCaMP brain wide, this correlation was comparable between closed and open loop conditions, was highest in posterior regions of dorsal cortex, and lower in more anterior regions (**Figures 2A and 2B**). In mice that expressed GcaMP6 in Tlx3 positive L5 IT neurons, the correlation between locomotion speed and calcium activity in the closed loop session was negative in posterior regions of dorsal cortex and positive in anterior regions. Conversely, in open loop conditions, the correlation was positive throughout dorsal cortex (**Figures 2C and 2D**). To test whether it was the coupling of visual flow that resulted in a reduction of the correlation in the closed loop condition or whether the presence of an uncoupled visual stimulus resulted in an increase of correlation, we also compared these correlations to those observed when mice were locomoting in relative darkness (see Methods). In C57BL/6 mice that expressed GCaMP brain wide the correlation of calcium activity with locomotion in darkness was indistinguishable from that in closed or open loop (**Figure 2B**). In mice that

expressed GCaMP6 in Tlx3 positive L5 IT neurons, an interesting pattern emerged. In visual regions of dorsal cortex, the correlation between locomotion speed and calcium activity in relative darkness resembled that observed in open loop conditions, while in frontal regions, it resembled that observed in closed loop conditions. In visual regions, the coupling of visual flow resulted in a reduction of correlation, while in frontal regions the presence of an uncoupled visual stimulus resulted in an increase of correlations. Thus, the difference between closed and open loop conditions likely had different origins in visual and frontal regions of dorsal cortex. Overall, we concluded that the coupling of locomotion and resulting visual flow feedback not only activated Tlx3 positive L5 IT neurons differentially but did so throughout dorsal cortex, well beyond visual regions.

Visuomotor prediction errors originated in visual cortical regions and had opposing effects on Tlx3 positive L5 IT activity

A consequence of the natural coupling of locomotion and visual flow feedback is that movements are a good predictor of self-generated sensory feedback. In our closed loop experiments, forward locomotion was a strong predictor of backward visual flow. It has been speculated that such predictions are used to compute prediction errors in layer 2/3 (L2/3) of cortex (Jordan and Keller, 2020). Prediction errors come in two variants: Positive prediction errors that signal more visual flow than predicted and negative prediction errors that signal less visual flow than predicted (Keller and Mrsic-Flogel, 2018; Rao and Ballard, 1999). To probe for negative and positive prediction error signals, we quantified the responses to visuomotor mismatch events and to visual stimuli (representing less and more visual flow input than expected, respectively). Visuomotor mismatch was introduced by briefly (1 s) halting visual flow during self-generated feedback in the closed loop condition. Visual responses were elicited by presenting drifting grating stimuli to a passively observing mouse (see Methods). Please note, both types of prediction errors can be probed using a variety of stimuli, but the two we are using here, in our experience, are the most robust at eliciting strong responses in V1. In C57BL/6 mice that expressed GCaMP brain wide, both visuomotor mismatch and grating stimuli resulted in increases of activity that were strongest and appeared first in visual regions of dorsal cortex (**Figures 3A-3C**). In mice that expressed GCaMP6 in Tlx3 positive layer 5 IT neurons, visuomotor mismatch resulted in an increase of activity in V1, while grating onset resulted in a decrease of activity in V1 (**Figures 3D-3F**). Thus, in dorsal cortex, both mismatch and drifting grating stimuli primarily activated visual cortex but resulted in opposing activation patterns in Tlx3 positive L5 IT neurons. An increase in activity to negative prediction errors and a decrease to positive prediction errors would be consistent with either a population of negative prediction error neurons or a type of internal representation neuron (Rao and Ballard, 1999). Given that L5 neurons

in V1 do not exhibit the opposing influence of top-down and bottom-up input necessary to compute prediction errors (Jordan and Keller, 2020), we speculated that Tlx3 positive L5 IT neurons might function as a type of internal representation neuron.

The antipsychotic drug clozapine alters visuomotor integration in L5

The activation of an internal representation is the brain's best guess at what the stimuli in the environment are. We speculated that the activation of such an internal representation would be particularly susceptible to substances that are known to reduce illusory percepts, like antipsychotic drugs. We thus quantified the changes in dorsal cortex activity associated with a single intraperitoneal injection of an antipsychotic drug (clozapine). In C57BL/6 mice that expressed GCaMP brain wide, we found that closed and open loop locomotion onsets were almost unaffected by clozapine (**Figures 4A and 4B**), while there was a small increase in open loop visual flow onset responses (**Figure 4C**). In mice that expressed GCaMP6 in Tlx3 positive L5 IT neurons, however, clozapine fundamentally changed both closed and open loop locomotion onset responses. In V1, both types of locomotion onset now resulted in a massive increase in activity (**Figures 4D and 4E**). Conversely, open loop visual flow onset responses remained largely unchanged (**Figure 4F**). Clozapine also had an opposing effect on the average correlation of activity with locomotion in Tlx3 positive L5 IT neurons. While the average correlation between activity and locomotion was increased in C57BL/6 mice that expressed GCaMP brain wide, the same measure was decreased in mice that expressed GCaMP6 in Tlx3 positive L5 IT neurons (**Figure S4**). Thus, consistent with the speculation that Tlx3 positive L5 neurons might function as internal representation neurons, clozapine exhibited a substantially stronger influence on locomotion onset responses in Tlx3 positive L5 IT neurons than would be expected from the effect of clozapine on brain wide responses.

Antipsychotic drugs decouple long-range cortico-cortical activity

L5 IT neurons are the primary source of long-range cortical communication and are one prominent source of locomotion related activity in V1 (Leinweber et al., 2017). Given that clozapine increased locomotion onset responses in L5 IT neurons in V1, we wondered whether clozapine might more generally change the long-range influence between L5 IT neurons. To investigate this possibility, we computed the correlations of calcium activity between the six regions of interest across both hemispheres and all recording conditions. We did this first in C57BL/6 mice that expressed GCaMP brain wide before (**Figure 5A**) and after a single intraperitoneal injection of clozapine (**Figure 5B**). Overall, clozapine resulted in a relatively modest decrease in correlations. On repeating this experiment in mice that expressed GCaMP6 in Tlx3 positive L5 IT neurons, we found a larger

decrease in correlations that appeared to be stronger for regions that were further apart (**Figures 5C and 5D**). To quantify these changes, we plotted the correlations as a function of linear distance between the regions as measured in a top-down view of dorsal cortex (**Figure S5A**). Note, this is of course only an approximation of the actual axonal path length between the regions. To visualize the distribution of correlations, we interpolated the data and represented them as heatmaps (**Figure S5B**). The resulting representation for the data from C57BL/6 mice that expressed GCaMP brain wide before and after clozapine injection is shown in **Figures 6A** and **6B**, respectively. We then split the data into approximately equal portions of short- and long-range correlations using a cutoff of 0.9 times the bregma-lambda distance (approx. 3.8 mm). While both short- and long-range correlations were reduced, this reduction was not significant in either case (**Figure 6C**). We also found no evidence of a difference between short- and long-range correlation changes. In mice that expressed GCaMP6 in Tlx3 positive layer 5 IT neurons, however, we found a significant reduction in both short- and long-range correlations (**Figures 6D and 6E**), and both were reduced stronger than in C57BL/6 mice that expressed GCaMP brain wide (C57BL/6 vs Tlx3-Cre x Ai148, short-range: $p < 0.05$; long-range: $p < 10^{-5}$; rank-sum test). Moreover, the reduction in activity correlations was stronger for long-range correlations than it was for short-range correlations (**Figure 6F**). To confirm that the clozapine induced reduction in correlation was stronger in deep cortical layers, we repeated the experiment in a population of L2/3 and L4 excitatory neurons using Cux2-CreERT2 x Ai148 mice. Consistent with the hypothesis that the strongest effect of clozapine was observed in L5 IT neurons, we found that clozapine decreased correlations of cortical activity in superficial excitatory neurons (**Figure S6**). However, this reduction was significantly weaker than the reduction we observed in mice that expressed GCaMP6 in Tlx3 positive layer 5 IT neurons (Cux2-CreERT2 x Ai148 vs Tlx3-Cre x Ai148, short-range: $p < 0.005$, long-range: $p < 10^{-8}$, rank-sum test). Thus, administration of the antipsychotic drug clozapine resulted in a decorrelation of activity across dorsal cortex that was stronger in L5 IT neurons (Tlx3) than it was in either L2/3 excitatory neurons (Cux2) or in the brain wide average (C57BL/6).

To test whether the decorrelation of the activity of L5 IT neurons is specific to clozapine or might more generally be a functional signature of antipsychotic drugs, we repeated the experiments with two additional antipsychotic drugs, aripiprazole and haloperidol. We found that the principal effect of decorrelation of the activity patterns of Tlx3 positive L5 IT neurons was preserved with both drugs (**Figures 7A-7F**). These changes in correlation were absent upon injection of a psychostimulant (amphetamine; **Figures 7G-7I**). Thus, it is possible that antipsychotic drugs in general might function by reducing the strength of long-range interactions between cortical L5 IT neurons.

Changes in the correlation between cortical regions could either be driven by changes in common external inputs or through changes in communication between them. If antipsychotic drugs primarily reduce correlations by reducing the strength of communication between cortical regions, we would expect to find changes in the way responses spread between cortical regions. We used visuomotor prediction error responses that originated in V1 (**Figure 3**) to quantify how the spread of these responses in Tlx3 positive layer 5 IT neurons was influenced by antipsychotic drugs. The computation of negative prediction errors during movement requires a prediction of visual flow, which is mediated by long-range cortical input from L5 neurons in regions like A24b (Leinweber et al., 2017), as well as a bottom-up visual signal. By contrast, the computation of a positive prediction error during passive observation requires, in principle, only a bottom-up visual signal (assuming a prediction of no-change is signaled as an absence of activity in top-down input). Thus, we would primarily expect to find a reduction in mismatch responses in layer 5 IT neurons and a reduction in the spread of this signal to secondary visual regions. This is indeed what we observed: Mismatch responses were partially reduced in V1 and almost absent in V2am after injection of antipsychotic drugs (**Figure 8A**). And while responses to onsets of drifting gratings were also reduced in V2am, they were overall less affected by the antipsychotic drugs than mismatch responses (**Figure 8B**). Why there would be a differential effect on the propagation of positive and negative prediction error responses from V1 to V2am is unclear. Nevertheless, these results are consistent with the interpretation that antipsychotic drugs reduce lateral communication in L5.

DISCUSSION

When interpreting our results, it should be kept in mind that the source of the widefield imaging signal in these experiments is not entirely clear and is likely a combination of somatic, dendritic, and axonal signals. Given that the signal attenuation half depth in cortex is on the order of 100 µm (Aravanis et al., 2007), most signals likely come from the superficial 100 µm of tissue (Allen et al., 2017). In the case of the Tlx3 recordings, this would mean that we were recording a mixture of axonal and dendritic signals of the Tlx3 neurons that have their soma in L5 but have a dense net of axons and dendrites in L1. In the case of the brain wide expression of GCaMP using an AAV-PHP.eB in C57BL/6 mice, the signals we recorded likely also include contributions from thalamic axons. In addition to this, there is a hemodynamic contribution to the signal (Allen et al., 2017; Ma et al., 2016; Valley et al., 2020) that is the result of varying occlusion by blood vessels. We attempted to correct for the hemodynamic response using a 405 nm wavelength isosbestic illumination of GCaMP6, but we have found that we cannot recover the hemodynamic responses measured in GFP experiments. Accurate correction likely requires calibration on GFP measurements (Valley et al.,

2020). Given that hemodynamic responses should not systematically differ between different mouse lines, and that in the crystal skull preparation the contribution of hemodynamic occlusion to increases in fluorescence were relatively small (**Figure S1**), these hemodynamic artefacts should not substantially alter our conclusions. Lastly, it should be kept in mind that responses in these widefield recordings inherently reflect population averages. Assuming there is some form of lateral inhibition among neurons, population averages need not reflect responses of neurons that are tuned to the specific stimulus presented. For example, the suppression to grating stimuli we observed in V1 Tlx3 positive L5 IT neurons could be the result of a subset of Tlx3 neurons that are strongly responsive to the specific grating presented suppressing the rest of the population of Tlx3 neurons. The sum of both could then result in a net decrease in calcium activity. Thus, an understanding of the mechanism that results in opposing population responses of Tlx3 positive L5 IT neurons to positive and negative prediction errors will require measurements with single neuron resolution.

In our experiments we have focused on Tlx3 positive L5 IT neurons, but given that L5 IT neurons are densely connected to L5 pyramidal tract neurons (Anderson et al., 2010; Kiritani et al., 2012) and to L6 neurons (Xu et al., 2016; Yamawaki and Shepherd, 2015), it is not unlikely that these neuron types would follow similar patterns of activity and exhibit similar susceptibility to the influence of antipsychotic drugs. In the comparison of closed and open loop locomotion onsets, we do indeed find that Ntsr1 positive L6 excitatory neurons exhibit similar levels of dissimilarity as those observed in Tlx3 positive L5 IT neurons (**Figure 1L**). It is possible that responses in the Ntsr1 recordings, however, were noisier than those in the Tlx3 recordings (**Figure S3**), likely because of the lower dendritic and axonal volume of Ntsr1 positive neurons in L1. Thus, while we have focused on the Tlx3 positive L5 IT neurons mainly for reasons of experimental convenience, it is possible that both the differential activation in closed and open loop locomotion onsets as well as the susceptibility of long-range correlations to antipsychotic drugs is a general feature of cortical layers 5 and 6.

It is still unclear what the relevant sites of action in the brain are of antipsychotic drugs. Antipsychotic drugs are often antagonists of the D2 receptors, which are most strongly expressed in striatum. Consequently, it is sometimes assumed that the relevant site of action of antipsychotics is the striatum. Consistent with this, an increase in striatal dopamine activates auditory cortex (Maia and Frank, 2017) and mediates hallucination-like perceptions in mice (Schmack et al., 2021). It is intriguing, however, to speculate that the effects we observed in L5 IT neurons, which provide a dominant input to striatum (Morita et al., 2019), may be an alternate site of action. Feedback from striatum to cortex is exclusively mediated through thalamus, and neither L4, the primary thalamo-recipient layer in cortex, nor our brain wide recordings exhibited any of the effects we saw in L5 IT

neurons. Thus, the effects we saw in L5 IT neurons are either not inherited from striatum or are mediated by a separate set of thalamic neurons via direct thalamic input to deep cortical layers (Constantinople and Bruno, 2013; Douglas and Martin, 1991). Thalamocortical collaterals in deep layers, however, come from thalamic neurons that project primarily to superficial layers (Oberlaender et al., 2012). Thus, we think it is unlikely that the observed effects in L5 IT neurons were inherited from striatum. Independent of whether the treatment-relevant site of action of antipsychotic drugs is indeed in L5 IT neurons, the long-range decorrelation of activity we observed after antipsychotic drug injection could be used as a basis for a functional screen for compounds with antipsychotic efficacy. Given that in the brain wide recordings the decorrelation of activity was weaker compared to that observed in Tlx3 positive L5 IT neurons, it might be possible to test for similar effects in human subjects using layer specific fMRI recordings (Haarsma et al., 2020).

A rather surprising implication of our results is that the dominant mode of coupling in cortex might be lateral, not vertical. Both the observation that the difference between closed and open loop locomotion onsets were detectable predominantly in L5 and that the antipsychotic drug induced decorrelation of dorsal cortex activity was predominantly evident in L5, suggest that the lateral coupling within L5 across dorsal cortex is stronger than the vertical coupling between superficial layers and L5.

One of the diseases treated with antipsychotic drugs is schizophrenia. It has been speculated that disrupted resting-state functional connectivity in brain networks involving cortex is central to the pathogenesis of schizophrenia (Li et al., 2017; Northoff and Duncan, 2016). Schizophrenic patients exhibit increases in resting state functional connectivity between a subset of cortical regions (Li et al., 2019). Auditory hallucinations, one of the hallmark symptoms of schizophrenia, are associated with increased activation of diverse cortical regions (Catafau et al., 1994; Dierks et al., 1999; Shergill et al., 2000). Thus, it is conceivable that antipsychotic drugs counteract this by reducing the strength of long-range cortical connectivity mediated by layer 5 IT neurons, independent of whether the increased activity in schizophrenic patients is indeed driven by aberrant increases in the strength of long-range cortical connections or is a consequence of an aberrant increase in the strength of striato-thalamo-cortical loops. However, a direct involvement of cortical circuits in the pathogenesis of schizophrenia is consistent with the glutamate hypothesis of schizophrenia. It is based on the finding that NMDA receptor antagonists induce schizophrenia-like symptoms (Moghaddam and Javitt, 2012), and that disturbances of NMDA and AMPA receptor related gene expression are associated with schizophrenia (Harrison and Weinberger, 2005; Singh et al., 2020). In V1, it has been shown that NMDA receptors are necessary during visual development to establish normal prediction

error signaling (Widmer and Keller, 2021). Thus, it is conceivable that a disruption of glutamatergic signaling in cortex that alters the way internal representations are activated by prediction errors is central to the etiology of schizophrenia. If so, we should find impairments in all domains of cortical function, including sensory processing. In the case of the sensory cortex, cortical dysfunctions should be apparent earlier in development, concurrent with the critical period for plasticity in sensory areas of cortex. While the core symptoms of schizophrenia typically appear in late adolescence, sensory processing is indeed impaired in schizophrenic patients (Javitt, 2009) and is apparent, for example, in the reduction of surround suppression in V1 (Yoon et al., 2009). Interestingly, some of these disturbances are detectable already during childhood as visuo-perceptual and reading anomalies in some subjects that later develop schizophrenia (Parellada et al., 2017). Positive symptoms of schizophrenia can be explained in a predictive processing framework of cortical function as a disturbance of a prediction error based update of internal representations (Fletcher and Frith, 2009; Frith, 2005). There are two types of prediction error neurons, positive and negative, and, given that cortex likely implements a non-hierarchical variant of predictive processing (Garner and Keller, 2022), two types of internal representation neurons. One set of internal representation neurons is excited by positive prediction errors and inhibited by negative prediction errors, and the other one is inhibited by positive prediction errors and excited by negative prediction errors (Keller and Mrsic-Flogel, 2018). Tlx3 positive L5 IT neurons exhibited opposing responses to positive and negative prediction errors (**Figure 3**), consistent with the responses of internal representation neurons. Given that the effects of antipsychotic drugs are predominantly observed in L5 IT neurons and that anesthesia is thought to decouple L5 neuron somata from their apical tuft and thereby prevents conscious perception (Suzuki and Larkum, 2020), we speculate that Tlx3 positive L5 IT neurons may be one type of internal representation neuron and one of the functionally relevant sites of antipsychotic action. Finally, it is possible that an aberrant pattern of functional connectivity among layer 5 cortical neurons is central to the pathogenesis of schizophrenia.

FIGURES

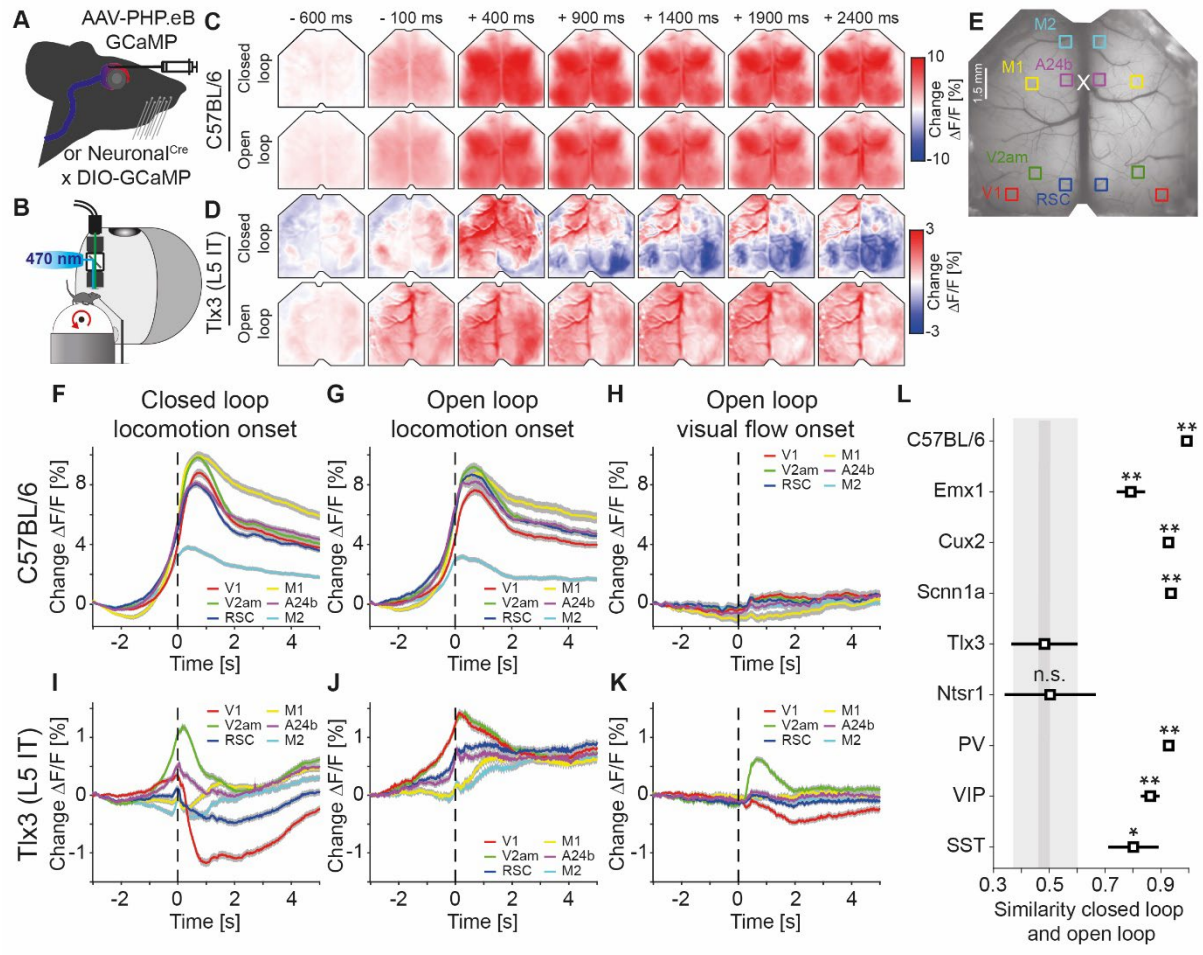

Figure 1. Activation patterns of deep cortical layers distinguished closed and open loop locomotion onsets throughout dorsal cortex.

(**A**) Schematic of GCaMP expression strategy. We either injected an AAV-PHP.eB virus retroorbitally to express GCaMP brain wide (C57BL/6), in cortical excitatory neurons (Emx1-Cre) or in a subset of SST positive interneurons (see Methods and **Table S2**) or used the progeny of a cross of a cell type specific Cre driver line (Neuronal^{Cre}: Cux2-CreERT2, Scnn1a-Cre, Tlx3-Cre, Ntsr1-Cre, PV-Cre, VIP-Cre or SST-Cre) with the Ai148 GCaMP6 reporter line. All mice were then implanted with a crystal skull cranial window prior to imaging experiments.

(**B**) Schematic of the experimental setup. We imaged GCaMP fluorescence under 470 nm LED illumination with an sCMOS camera through a macroscope. Mice were free to locomote on an air supported spherical treadmill while coupled (closed loop), uncoupled (open loop), or no (dark) visual flow in the form of movement along a virtual corridor was displayed on a toroidal screen placed in front of the mouse. Walls of the virtual corridor were patterned with vertical sinusoidal gratings. In a separate condition, we then presented drifting grating stimuli (grating session, see Methods).

(**C**) Average response in an example C57BL/6 mouse that expressed GCaMP6 brain wide during closed loop locomotion onsets (top row, 83 onsets) and open loop locomotion onsets (bottom row, 153 onsets). Locomotion onsets in both conditions activated dorsal cortex similarly.

(**D**) As in **C**, but in an example Tlx3-Cre x Ai148 mouse that expressed GCaMP6 in L5 IT neurons during closed loop locomotion onsets (top row, 88 onsets) and open loop locomotion onsets (bottom row, 83 onsets). Note that activity decreased in posterior regions of dorsal cortex during closed loop locomotion onsets.

(**E**) Example crystal skull craniotomy marking the 6 regions of interest in each hemisphere we selected: primary visual cortex (V1, red), retrosplenial cortex (RSC, blue), antero-medial secondary visual cortex (V2am, green), primary motor cortex (M1, yellow), anterior cingulate cortex (A24b, purple), and secondary motor cortex (M2, cyan). The white cross marks bregma.

(**F**) Average response during closed loop locomotion onsets in C57BL/6 mice that expressed GCaMP brain wide in the 6 regions of interest (907 onsets in 6 mice, activity was averaged across corresponding regions in both hemispheres). Shading indicates SEM over onsets.

(**G**) As in **F**, but for open loop locomotion onsets (598 onsets in 6 mice).

(**H**) As in **F**, but for visual flow onsets in the open loop condition restricted to times when the mice were not locomoting (416 onsets in 6 mice).

(**I**) Average response during closed loop locomotion onsets in Tlx3-Cre x Ai148 mice that expressed GCaMP6 in L5 IT neurons (1919 onsets in 15 mice, activity was averaged across corresponding regions in both hemispheres). Shading indicates SEM over onsets.

(**J**) As in **I**, but for open loop locomotion onsets (1125 onsets in 15 mice).

(**K**) As in **J**, but for visual flow onsets during open loop sessions restricted to times when the mice were not locomoting (1189 onsets in 15 mice).

(**L**) Similarity of the average closed loop and open loop locomotion onset responses quantified as the correlation coefficient between the two in a window -5 s to +3 s around locomotion onset (see Methods). Error bars indicate SEM over the 12 (6 per hemisphere) cortical regions. Statistical comparisons are against the Tlx3 data: n.s.: not significant, *: $p < 0.05$, **: $p < 0.01$. See **Table S1** for all information on statistical testing.

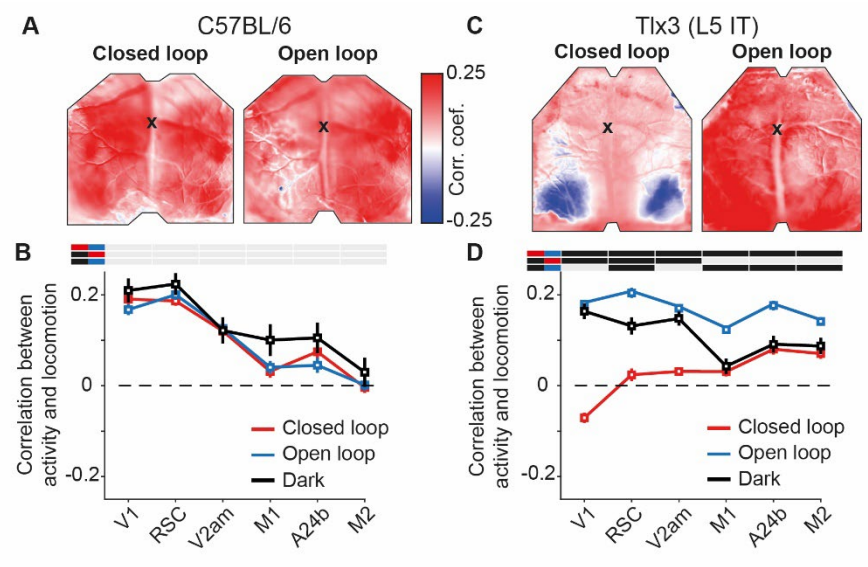

Figure 2. L5 IT neurons were differentially activated by locomotion depending on the type of visual feedback.

(**A**) Correlation between calcium activity and locomotion speed in the closed loop (left) and open loop (right) conditions, calculated for each pixel in the image for one example C57BL/6 mouse that expressed GCaMP brain wide. The black cross marks bregma. Activity in most of dorsal cortex correlates positively with locomotion in both closed and open loop conditions.

(**B**) Average correlation between calcium activity and locomotion speed in the 6 regions of interest in closed loop (red), open loop (blue) or dark (black) conditions in 6 C57BL/6 mice that expressed GCaMP brain wide (308, 316, and 68 5-minute sessions, respectively). Error bars indicate SEM over sessions. Bars above the plot indicate significant differences between conditions (compared conditions are indicated by colored line segments to the left, black: $p < 0.05$, gray: n.s., see **Table S1** for all information on statistical testing). On average, the correlation was highest in posterior dorsal cortex and was not different between conditions.

(**C**) As in **A**, but for an example Tlx3-Cre x Ai148 mouse that expressed GCaMP6 in L5 IT neurons. Correlations of calcium activity and locomotion speed were lower in the closed loop condition compared to the open loop condition, most prominently so in posterior regions of dorsal cortex.

(**D**) As in **B**, but for 15 Tlx3-Cre x Ai148 mice that expressed GCaMP6 in L5 IT neurons (data from 420 closed loop, 394 open loop and 194 dark 5-minute sessions). Error bars indicate SEM over sessions. Correlation differed significantly between the closed loop and the open loop condition and was lowest in posterior dorsal cortex during the closed loop condition.

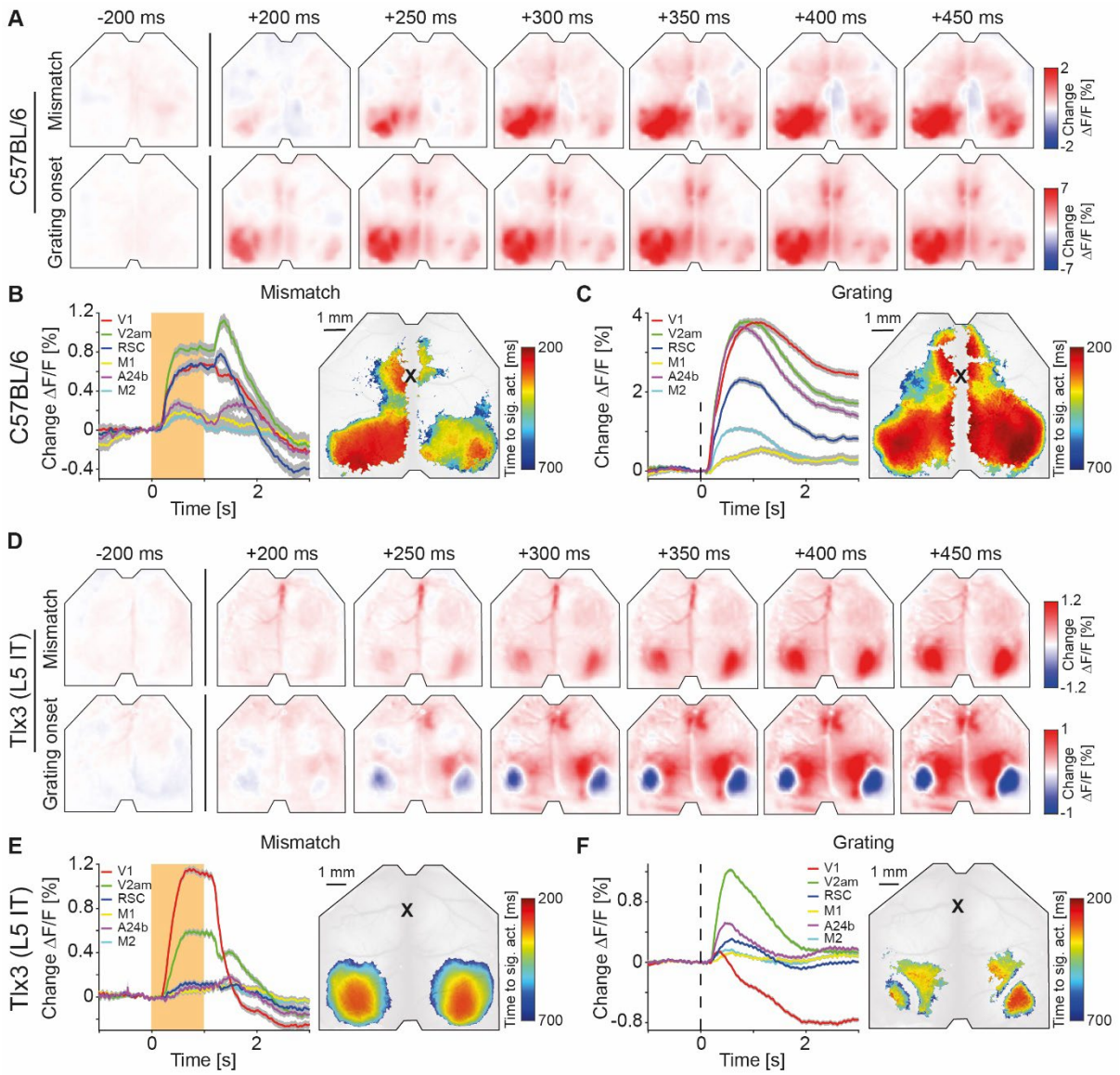

454 **Figure 3. Visuomotor prediction error responses in dorsal cortex originated in V1 and activated L5**
455 **IT neurons differentially.**

456 (**A**) Average responses to mismatch (230 onsets, top row) and drifting gratings (86 onsets, bottom
457 row) in an example C57BL/6 mouse that expressed GCaMP6 brain wide.

458 (**B**) Left: Average response to mismatch in C57BL/6 mice that expressed GCaMP brain wide (2512
459 onsets in 6 mice, activity was averaged across corresponding regions in both hemispheres). Shading
460 indicates SEM over onsets. Orange shading indicates duration of mismatch event. Right: Average
461 time to significant activation to mismatch in 6 C57BL/6 mice (see Methods), overlayed onto an
462 example image of a craniotomy. Black cross marks bregma.

463 (**C**) As in **B**, but for drifting grating responses (1858 onsets in 6 mice).

464 (**D**) As in **A**, but in an example Tlx3-Cre x Ai148 mouse that expressed GCaMP6 in L5 IT neurons
465 (mismatch, 292 onsets, top row; drifting gratings, 171 onsets, bottom row).

(**E**) As in **B**, but for Tlx3-Cre x Ai148 mice that expressed GCaMP6 in L5 IT neurons (3297 onsets in 15 mice).

(**F**) As in **C**, but for Tlx3-Cre x Ai148 mice that expressed GCaMP6 in L5 IT neurons (5318 onsets in 15 mice).

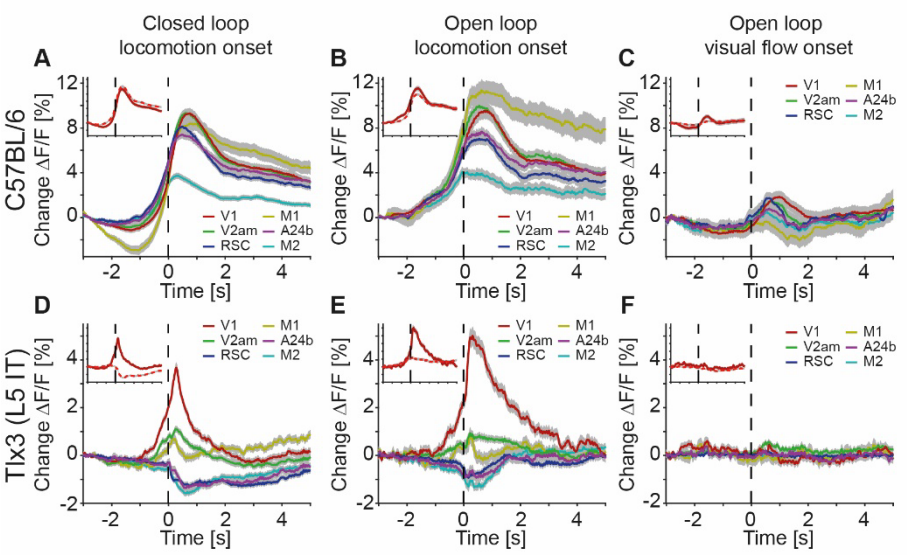

Figure 4. Clozapine increased locomotion related responses in L5 IT neurons in V1.

(**A**) Average response during closed loop locomotion onsets in C57BL/6 mice that expressed GCaMP brain wide (273 onsets in 4 mice, activity was averaged across corresponding regions in both hemispheres) after a single injection of the antipsychotic drug clozapine (see Methods). Shading indicates SEM over onsets. Inset: Comparison of responses for V1 in 4 naive C57BL/6 mice (dashed red, 720 onsets) and the same 4 mice after clozapine injection (dark red, same data as in main panel).

(**B**) As in **A**, but for open loop locomotion onsets after clozapine injection (145 onsets in 4 mice; inset: 570 onsets in the same 4 mice before injection).

(**C**) As in **A**, but for open loop visual flow onsets restricted to times when the mice were not locomoting (99 onsets in 4 mice; inset: 404 onsets in the same 4 mice before injection).

(**D**) Average response during closed loop locomotion onsets in Tlx3-Cre x Ai148 mice that expressed GCaMP6 in layer 5 IT neurons (707 onsets in 5 mice, activity was averaged across corresponding regions in both hemispheres) after a single injection of the antipsychotic drug clozapine (see Methods). Shading indicates SEM over onsets. Inset: Comparison of responses for V1 in 5 naive Tlx3-Cre x Ai148 mice (dashed red, 1101 onsets) and the same 5 mice after clozapine injection (dark red, same data as in main panel).

(**E**) As in **D**, but for open loop locomotion onsets (350 onsets in 5 mice; inset: 348 onsets in the same 5 mice before injection).

(**F**) As in **D**, but for open loop visual flow onsets restricted to times when the mice were not locomoting (514 onsets in 5 mice; inset: 568 onsets in the same 5 mice before clozapine injection).

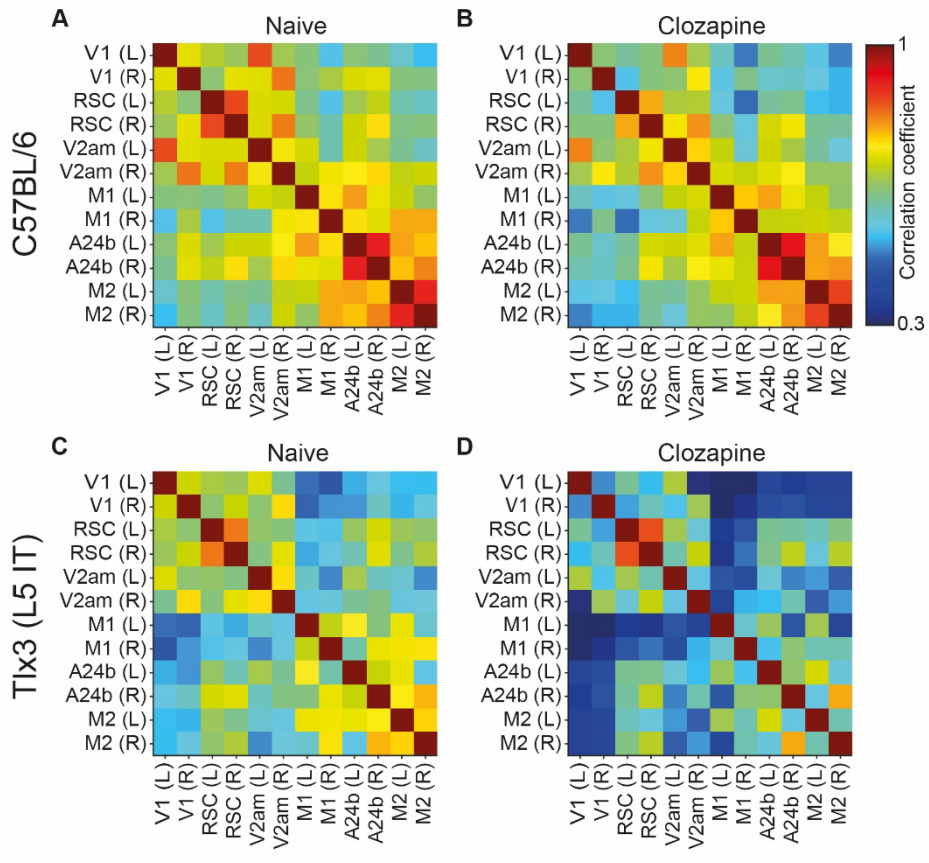

Figure 5. Clozapine reduced activity correlations in dorsal cortex predominantly in L5 IT neurons.

(**A**) Average correlation of activity between the 12 regions of interest in 4 C57BL/6 mice that expressed GCaMP brain wide.

(**B**) As in **A**, but after a single injection of the antipsychotic drug clozapine in the same 4 C57BL/6 mice.

(**C**) Average correlation of activity between the 12 regions of interest in 5 Tlx3-Cre x Ai148 mice that expressed GCaMP6 in layer 5 IT neurons.

(**D**) As in **C**, but after a single injection of the antipsychotic drug clozapine in the same 5 Tlx3-Cre x Ai148 mice.

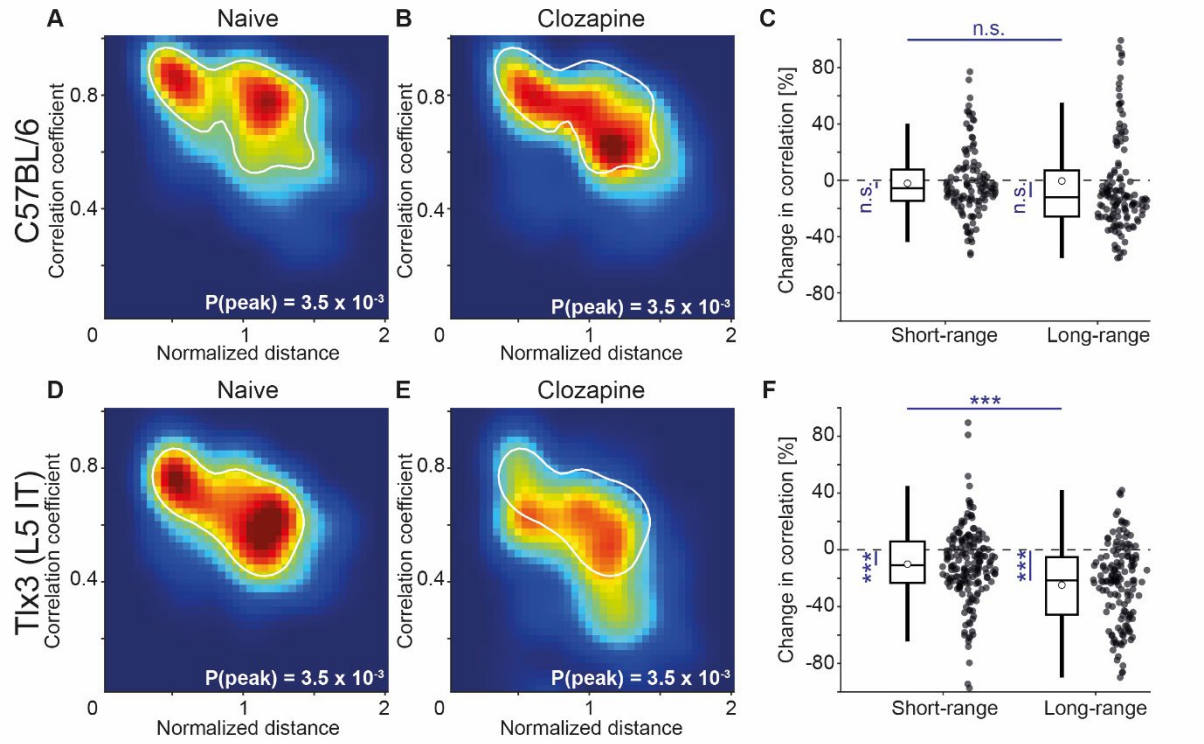

507 **Figure 6. L5 IT neurons exhibited the strongest clozapine induced reduction of long-range**
508 **correlations.**

509 (**A**) Density map of correlation coefficients as a function of distance between the regions, normalized
510 across mice by the bregma-lambda distance (see **Figure S5** and Methods), for 4 naive C57BL/6 mice
511 that expressed GCaMP brain wide. Peak density is indicated at the bottom right of the plot and
512 corresponds to the maximum value of the color scale (dark red). The white line is a contour line
513 drawn at 50% of peak value.

514 (**B**) As in **A**, but for the same 4 C57BL/6 mice after a single injection of the antipsychotic drug
515 clozapine. The white line is the contour line from panel **A** for comparison.

516 (**C**) Clozapine induced change in the activity correlation between regions, normalized to the
517 correlation coefficient in the naive state, in 4 C57BL/6 mice. Data were split into short- and long-
518 range activity correlations (see Methods). Boxes represent the median and the interquartile range.
519 The open circle indicates the mean of the distribution. The whiskers mark 1.5 times the interquartile
520 range. Dots are the individual data points (short-range: 122 pairs, long-range: 142 pairs). n.s.: not
521 significant. See **Table S1** for all information on statistical testing.

522 (**D**) As in **A**, but for 5 Tlx3-Cre x Ai148 mice that expressed GCaMP6 in layer 5 IT neurons.

523 (**E**) As in **B**, but for 5 Tlx3-Cre x Ai148 mice that expressed GCaMP6 in layer 5 IT neurons. The white
524 line is the contour line from panel **D** for comparison.

525 (**F**) As in **C**, but for 5 Tlx3-Cre x Ai148 mice that expressed GCaMP6 in layer 5 IT neurons (short-range:
526 182 pairs, long-range: 148 pairs). ***: $p < 0.001$.

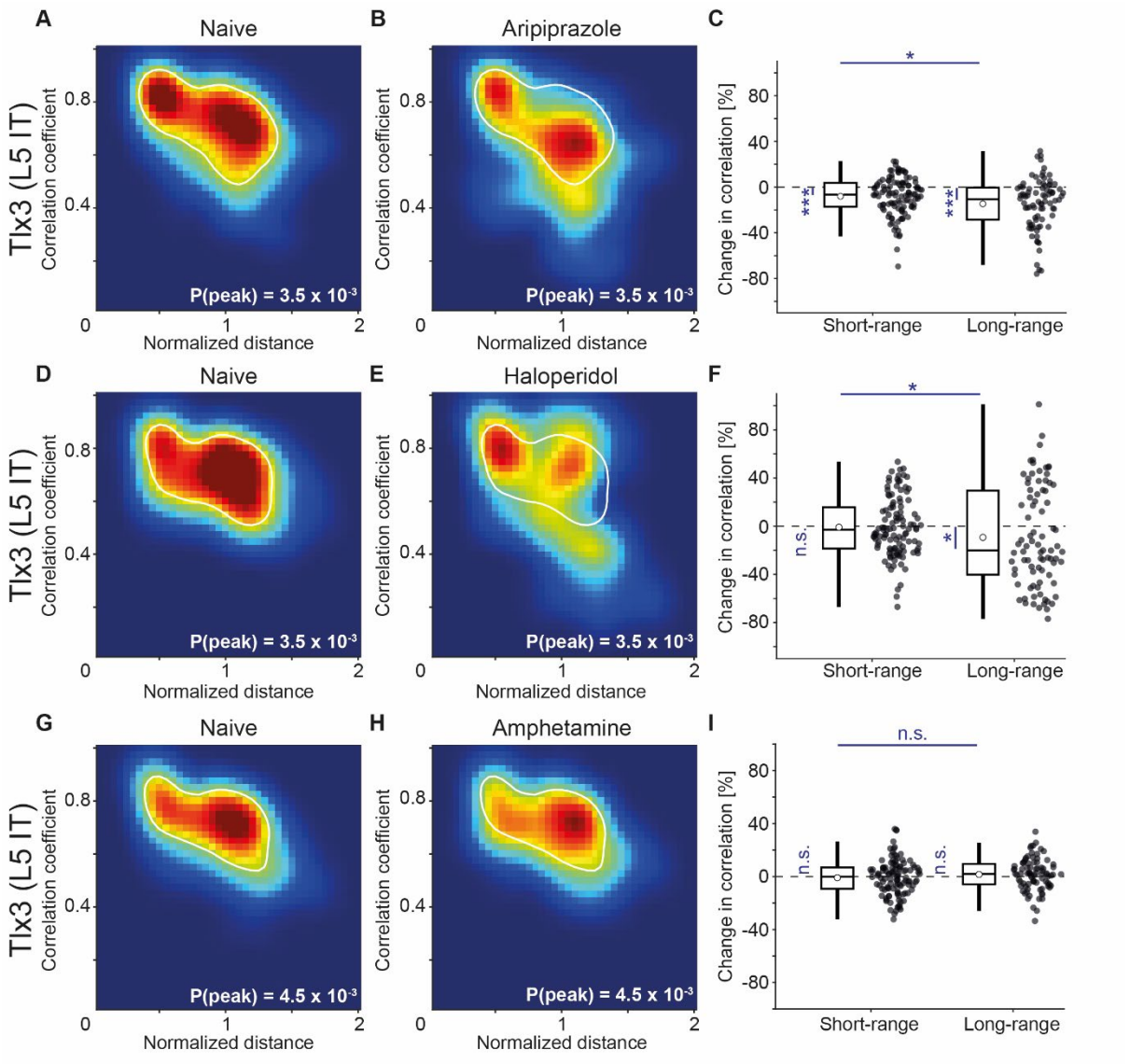

530 (**A**) Density map of correlation coefficients as a function of distance between the regions, normalized
531 across mice by the bregma-lambda distance (see **Figure S5** and Methods), for 3 Tlx3-Cre x Ai148
532 mice that expressed GCaMP6 in layer 5 IT neurons. Peak density is indicated at the bottom right of
533 the plot and corresponds to the maximum value of the color scale (dark red). The white line is a
534 contour line drawn at 50% of peak value.

535 (**B**) As in **A**, for the same 3 Tlx3-Cre x Ai148 mice, but after a single injection of the antipsychotic drug
536 aripiprazole. The white line is the contour line from panel **A** for comparison.

537 (**C**) Aripiprazole induced change in the activity correlation between regions, normalized to the
538 correlation coefficient in the naive state, in 3 Tlx3-Cre x Ai148 mice. Data were split into short- and
539 long-range activity correlations (see Methods). Boxes represent the median and the interquartile
540 range. The open circle indicates the mean of the distribution. The whiskers mark 1.5 times the

interquartile range. Dots are the individual data points (short-range: 114 pairs, long-range: 84 pairs). *: $p < 0.05$, ***: $p < 0.001$. See **Table S1** for all information on statistical testing.

(**D**) As in **A**, but for 3 different Tlx3-Cre x Ai148 mice.

(**E**) As in **D**, for the same 3 Tlx3-Cre x Ai148 mice, but after a single injection of the antipsychotic drug haloperidol. The white line is the contour line from panel **D** for comparison.

(**F**) As in **C**, but for the 3 mice that had received a single injection of the antipsychotic drug haloperidol (short-range: 114 pairs, long-range: 84 pairs). *: $p < 0.05$; n.s.: not significant.

(**G**) As in **A**, but for 3 different Tlx3-Cre x Ai148 mice.

(**H**) As in **G**, for the same 3 Tlx3-Cre x Ai148 mice, but after a single injection of the psychostimulant amphetamine. The white line is the contour line from panel **G** for comparison.

(**I**) As in **D**, but for the 3 mice that had received a single injection of the psychostimulant amphetamine (short-range: 114 pairs, long-range: 84 pairs). n.s.: not significant.

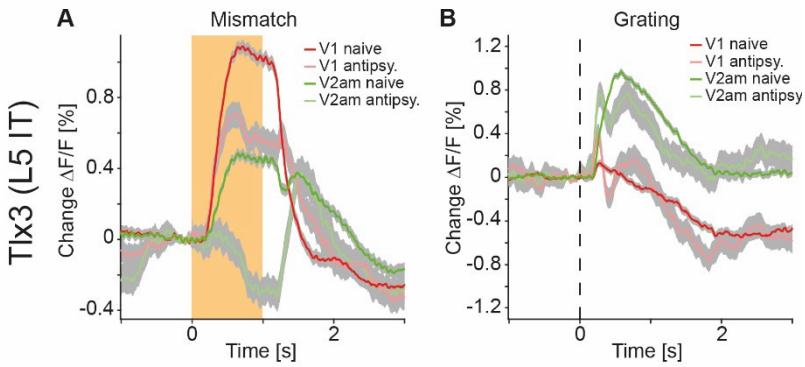

555 **Figure 8. Antipsychotic drug treatment reduced responses to and propagation of negative**
556 **prediction errors.**

557 (**A**) Average responses to mismatch in Tlx3-Cre x Ai148 mice that expressed GCaMP6 in layer 5 IT
558 neurons before (red: V1 naive, green: V2am naive, activity was averaged across corresponding
559 regions in both hemispheres) and after (pale red: V1, pale green: V2am) injection of a single dose of
560 an antipsychotic drug (data were averaged over all antipsychotics used: Clozapine: 5 mice,
561 aripiprazole: 3 mice, and haloperidol: 3 mice). Orange shading indicates duration of mismatch event.
562 Gray shading indicates SEM over onsets (naive: 2464 onsets, antipsychotic: 2017 onsets).

563 (**B**) As in **A**, but for drifting grating onsets (naive: 3942 onsets, antipsychotic: 1645 onsets).

564

SUPPLEMENTAL FIGURES

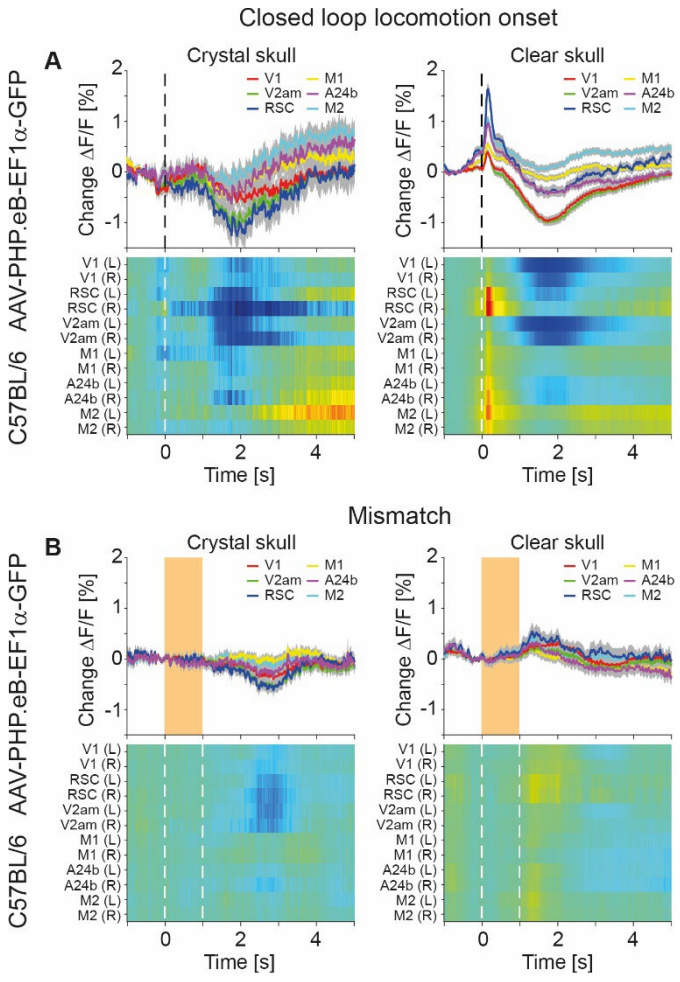

Figure S1. Hemodynamic responses were reduced in a crystal skull preparation compared to a clear skull preparation. Related to Figure 1.

(**A**) Average responses during closed loop locomotion onsets in C57BL/6 mice that expressed GFP brain wide using a crystal skull preparation (left: 3 mice, 96 locomotion onsets) or in similarly transfected mice using a clear skull preparation (right: 5 mice, 615 locomotion onsets) (see Methods). Top row shows the average activity of corresponding regions in dorsal cortex. Shading indicates SEM over onsets. The heatmaps in the bottom row show the responses for individual regions of interest. Heatmaps are scaled to the y-axis limits of the plot above (blue low, red high). Note, the fast onset transient apparent in the clear skull preparation was absent in the crystal skull preparation, while the slow decrease of activity was present in both. The increase in fluorescence at locomotion onset, which was primarily apparent in the clear skull preparation, is driven by hemodynamic occlusion.

(**B**) As in **A**, but for mismatch (left: 3 mice, 229 onsets, right: 5 mice, 228 onsets). Orange shading (top) or white dashed lines (bottom) indicate the duration of the mismatch stimulus.

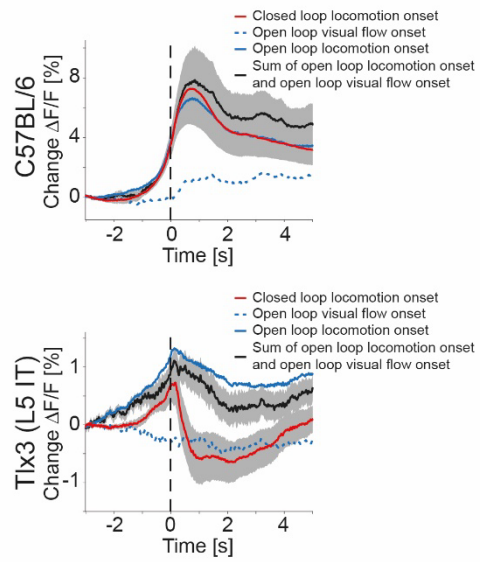

582 **Figure S2. The sum of locomotion and visual flow onset could not explain the closed loop**
583 **locomotion onset response of L5 IT neurons. Related to Figure 1.**

584 Average responses during closed (red) and open loop (blue) locomotion onsets, as well as open loop
585 visual flow (dashed blue) onsets, and the sum of open loop locomotion and open loop visual flow
586 onsets (black). In C57BL/6 mice that expressed GCaMP brain wide (top, 6 mice), closed loop
587 locomotion onset responses were larger than open loop locomotion onset responses, and part of
588 this difference could be explained by the visual flow onset responses. In Tlx3-Cre x Ai148 that
589 expressed GCaMP6 in layer 5 IT neurons (bottom, 15 mice), closed loop locomotion onset responses
590 cannot be explained as the sum of open loop locomotion and visual flow onset. Shading indicates
591 SEM over mice (omitted from open loop responses for clarity).

592

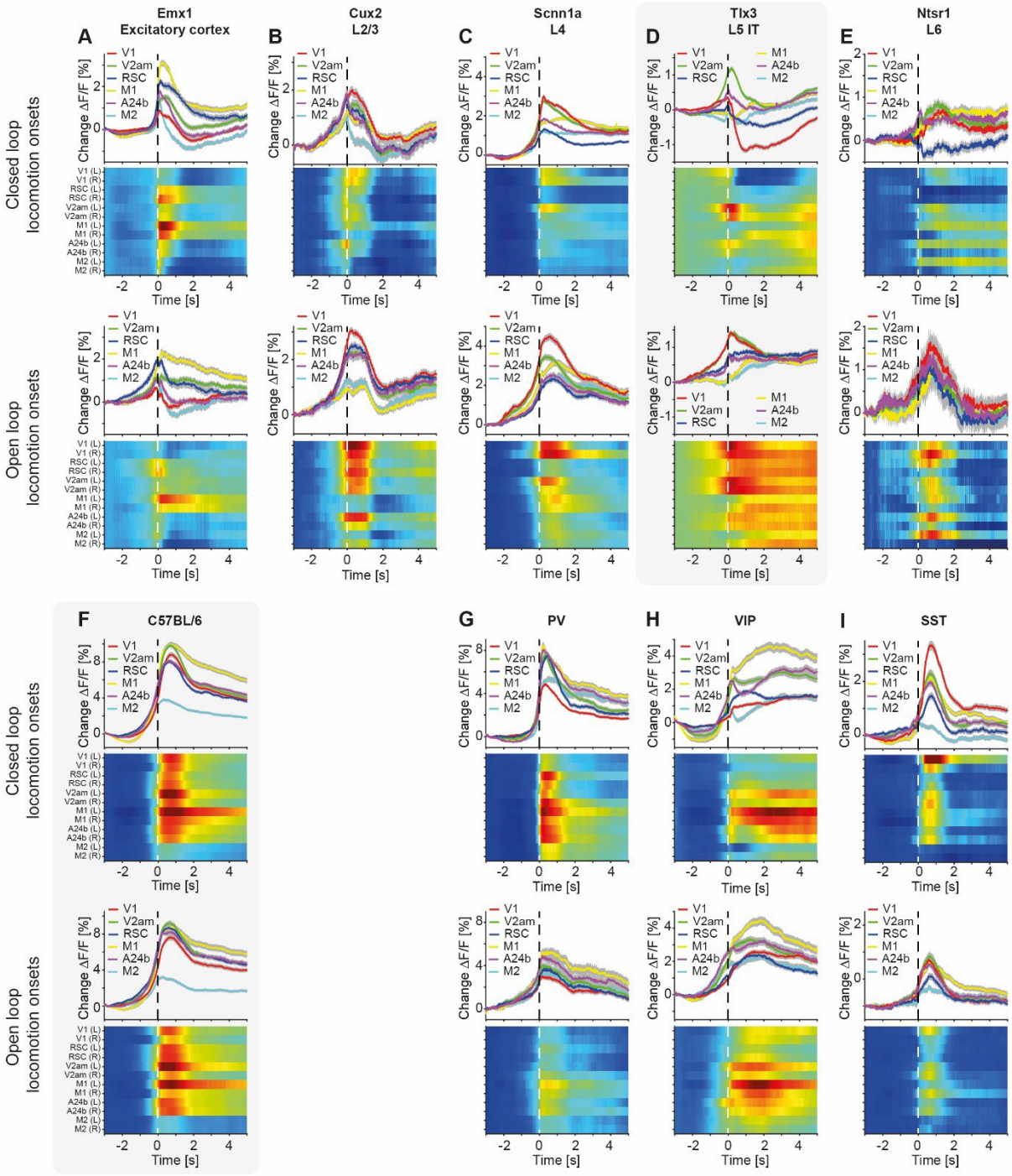

595 **Figure S3. L5 IT neurons had strikingly different responses during closed and open loop locomotion**
596 **onsets compared to other cortical neuron types. Related to Figure 1.**

597 (**A**) Average response during closed loop locomotion onsets (top, 438 onsets) and open loop
598 locomotion onsets (bottom, 286 onsets) in 4 Emx1-Cre mice that expressed GCaMP6 in excitatory
599 cortical neurons. Shading indicates SEM over onsets. Heatmaps are scaled to the y-axis limits of the
600 plot above (blue low, red high).

(**B**) As in **A**, but for 4 Cux2-CreERT2 x Ai148 mice that expressed GCaMP6 predominantly in L2/3 excitatory neurons (415 closed loop and 433 open loop locomotion onsets).

(**C**) As in **A**, but for 7 Scnn1a-Cre x Ai148 mice that expressed GCaMP6 in L4 excitatory neurons (839 closed loop and 313 open loop locomotion onsets).

(**D**) As in **A**, but for 15 Tlx3-Cre x Ai148 mice that expressed GCaMP6 specifically in L5 IT neurons (1919 closed loop and 1125 open loop locomotion onsets). Data are the same as in **Figures 1I and 1K**.

(**E**) As in **A**, but for 3 Ntsr1-Cre x Ai148 mice that expressed GCaMP6 in excitatory L6 neurons (368 closed loop and 112 open loop locomotion onsets).

(**F**) As in **A**, but for 6 C57BL/6 mice that expressed GCaMP brain wide (907 closed loop and 598 open loop locomotion onsets). Data are the same as in **Figures 1F and 1G**.

(**G**) As in **A**, but for 2 PV-Cre x Ai148 mice that expressed GCaMP6 in PV neurons (236 closed loop and 110 open loop locomotion onsets).

(**H**) As in **A**, but for 6 VIP-Cre x Ai148 mice that expressed GCaMP6 in VIP neurons (618 closed loop and 376 open loop locomotion onsets)

(**I**) As in **A**, but for 5 SST-Cre mice that expressed GCaMP6 in SST neurons (747 closed loop and 558 open loop locomotion onsets).

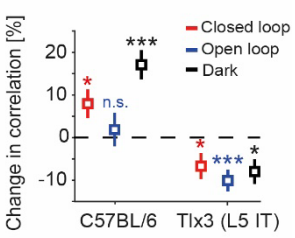

620 **Figure S4. Clozapine reduced the correlation between activity and locomotion in L5 IT neurons.**
621 **Related to Figure 4.**

622 Average correlation of activity and locomotion in dorsal cortex was increased after a single injection
623 of the antipsychotic drug clozapine in 4 C57BL/6 mice that expressed GCaMP brain wide but
624 decreased in 5 Tlx3-Cre x Ai148 mice that expressed GCaMP6 in layer 5 IT neurons, for all types of
625 visual feedback. Error bars indicate SEM over mice and corresponding dorsal cortex regions (see
626 Methods). n.s.: not significant, *: $p < 0.05$, ***: $p < 0.001$. See **Table S1** for all information on
627 statistical testing.

628

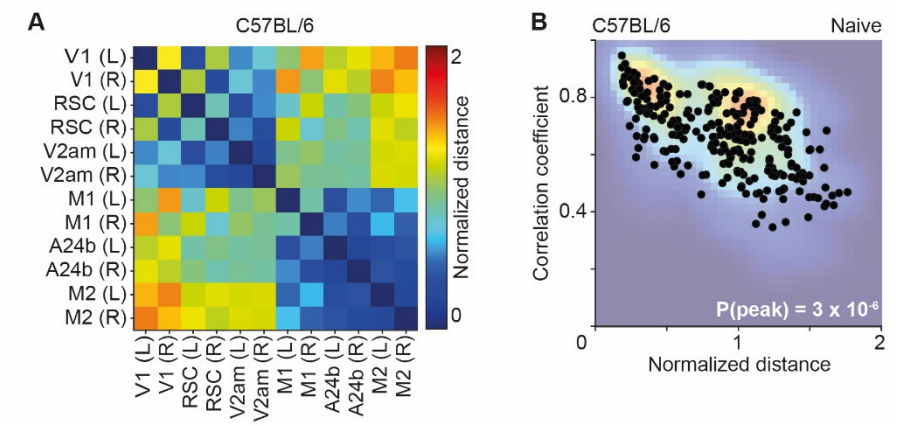

630 **Figure S5. Calculation of the distance-correlation heatmaps. Related to Figure 5.**

631 (**A**) For each pair of dorsal cortex regions, we calculated the distance between the regions in a top-
632 down view of dorsal cortex, normalized by the distance between bregma and lambda for each
633 mouse (data are from an example C57BL/6 mouse that expressed GCaMP6 brain wide).

634 (**B**) For each pair, we then plotted the activity correlation against this distance as calculated in **A**
635 (black dots). We then interpolated this distribution using a 40-by-40 2D grid to obtain the density
636 plots (faded background), shown for all mice and pairs in **Figures 5, 6 and S6**.

637

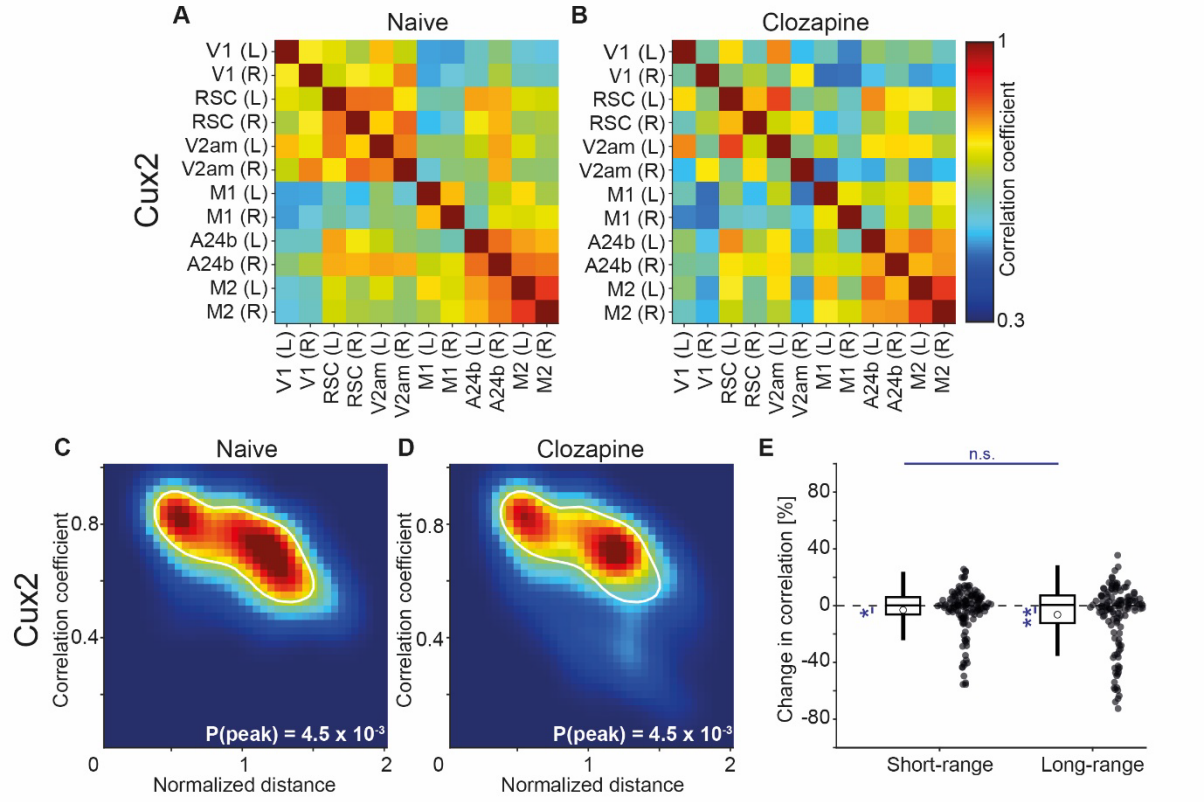

Figure S6. The clozapine induced decorrelation of dorsal cortex activity was weaker in superficial cortical layers than in L5. Related to Figure 5.

(**A**) Average correlation of activity between the 12 regions of interest in 4 Cux2-CreERT2 x Ai148 mice that expressed GCaMP6 predominantly in layer 2/3 excitatory cortical neurons.

(**B**) As in **A**, but for the same 4 Cux2-CreERT2 x Ai148 mice after a single injection of the antipsychotic drug clozapine.

(**C**) Density map of correlation coefficients as a function of distance between the regions, normalized across mice by the bregma-lambda distance (see **Figure S5** and Methods), for 4 naive Cux2-CreERT2 x Ai148 mice that expressed GCaMP6 predominantly in layer 2/3 cortical neurons. Peak density is indicated at the bottom right of the plot and corresponds to the maximum value of the color scale (dark red). The white line is a contour line drawn at 50% of peak value.

(**D**) As in **C**, but for the same 4 Cux2-CreERT2 x Ai148 mice after a single injection of the antipsychotic drug clozapine. The white line is the contour line from panel **C** for comparison.

(**E**) Clozapine induced change in the activity correlation between regions, normalized to the correlation coefficient in the naive state, in 4 Cux2-CreERT2 x Ai148 mice. Data were split into short- and long-range activity correlations (see Methods). Boxes represent the median and the interquartile range. The open circle indicates the mean of the distribution. The whiskers mark 1.5 times the interquartile range. Dots are the individual data points (short-range: 122 pairs, long-range: 142 pairs). n.s.: not significant, *: $p < 0.05$, **: $p < 0.01$. See **Table S1** for all information on statistical testing.

SUPPLEMENTAL TABLES

Table S1. Statistical comparisons for bar and violin plots.

Figure reference	Description (N_1 vs N_2)	Test	N_1 (mice)	N_2 (mice)	Unit	P-value
Figure 1L	Tlx3 vs C57BL/6	T-test	12 (15)	12 (6)	Regions	0.0012
	Tlx3 vs Emx1	T-test	12 (15)	12 (4)	Regions	0.0019
	Tlx3 vs Cux2	T-test	12 (15)	12 (4)	Regions	0.0045
	Tlx3 vs Scnn1a	T-test	12 (15)	12 (7)	Regions	0.0025
	Tlx3 vs Ntsr1	T-test	12 (15)	12 (3)	Regions	0.9175
	Tlx3 vs PV	T-test	12 (15)	12 (2)	Regions	0.0033
	Tlx3 vs VIP	T-test	12 (15)	12 (6)	Regions	0.0080
	Tlx3 vs SST	T-test	12 (15)	12 (5)	Regions	0.0384
Figure 2B	V1					
	Closed loop vs open loop	Rank-sum	308 (6)	316 (6)	Sessions	0.1088
	Closed loop vs dark	Rank-sum	308 (6)	68 (6)	Sessions	0.4131
	Open loop vs dark	Rank-sum	316 (6)	68 (6)	Sessions	0.1064
	RSC					
	Closed loop vs open loop	Rank-sum	308 (6)	316 (6)	Sessions	0.5522
	Closed loop vs dark	Rank-sum	308 (6)	68 (6)	Sessions	0.0786
	Open loop vs dark	Rank-sum	316 (6)	68 (6)	Sessions	0.2343
	V2am					
	Closed loop vs open loop	Rank-sum	308 (6)	316 (6)	Sessions	0.7924
	Closed loop vs dark	Rank-sum	308 (6)	68 (6)	Sessions	0.8326
	Open loop vs dark	Rank-sum	316 (6)	68 (6)	Sessions	0.9669
	M1					
	Closed loop vs open loop	Rank-sum	308 (6)	316 (6)	Sessions	0.9640
	Closed loop vs dark	Rank-sum	308 (6)	68 (6)	Sessions	0.0974
	Open loop vs dark	Rank-sum	316 (6)	68 (6)	Sessions	0.1597
	A24b					
	Closed loop vs open loop	Rank-sum	308 (6)	316 (6)	Sessions	0.1549
	Closed loop vs dark	Rank-sum	308 (6)	68 (6)	Sessions	0.4190
	Open loop vs dark	Rank-sum	316 (6)	68 (6)	Sessions	0.1540
	M2					
	Closed loop vs open loop	Rank-sum	308 (6)	316 (6)	Sessions	0.7265
	Closed loop vs dark	Rank-sum	308 (6)	68 (6)	Sessions	0.6720
	Open loop vs dark	Rank-sum	316 (6)	68 (6)	Sessions	0.6075
Figure 2D	V1					
	Closed loop vs open loop	Rank-sum	420 (15)	394 (15)	Sessions	$<10^{-10}$
	Closed loop vs dark	Rank-sum	420 (15)	194 (15)	Sessions	$<10^{-10}$
	Open loop vs dark	Rank-sum	394 (15)	194 (15)	Sessions	0.6851
	RSC					
	Closed loop vs open loop	Rank-sum	420 (15)	394 (15)	Sessions	$<10^{-10}$
	Closed loop vs dark	Rank-sum	420 (15)	194 (15)	Sessions	$<10^{-4}$
	Open loop vs dark	Rank-sum	394 (15)	194 (15)	Sessions	0.0010
	V2am					
	Closed loop vs open loop	Rank-sum	420 (15)	394 (15)	Sessions	$<10^{-10}$
	Closed loop vs dark	Rank-sum	420 (15)	194 (15)	Sessions	$<10^{-9}$
	Open loop vs dark	Rank-sum	394 (15)	194 (15)	Sessions	0.1570
	M1					
	Closed loop vs open loop	Rank-sum	420 (15)	394 (15)	Sessions	$<10^{-9}$
	Closed loop vs dark	Rank-sum	420 (15)	194 (15)	Sessions	0.5668
	Open loop vs dark	Rank-sum	394 (15)	194 (15)	Sessions	$<10^{-4}$

	A24b					
	Closed loop vs open loop	Rank-sum	420 (15)	394 (15)	Sessions	$<10^{-7}$
	Closed loop vs dark	Rank-sum	420 (15)	194 (15)	Sessions	0.6103
	Open loop vs dark	Rank-sum	394 (15)	194 (15)	Sessions	0.0001
	M2					
	Closed loop vs open loop	Rank-sum	420 (15)	394 (15)	Sessions	$<10^{-4}$
	Closed loop vs dark	Rank-sum	420 (15)	194 (15)	Sessions	0.5034
	Open loop vs dark	Rank-sum	394 (15)	194 (15)	Sessions	0.0111
Figure 6C	Short-range vs no change	T-test	122 (4)	-	Pairs	0.3791
	Long-range vs no change	T-test	142 (4)	-	Pairs	0.9035
	Short-range vs long-range	Rank-sum	122 (4)	142 (4)	Pairs	0.0511
Figure 6F	Short-range vs no change	T-test	182 (5)	-	Pairs	$<10^{-5}$
	Long-range vs no change	T-test	148 (5)	-	Pairs	$<10^{-10}$
	Short-range vs long-range	Rank-sum	182 (5)	148 (5)	Pairs	$<10^{-4}$
Figure 7C	Short-range vs no change	T-test	114 (3)	-	Pairs	$<10^{-5}$
	Long-range vs no change	T-test	84 (3)	-	Pairs	$<10^{-7}$
	Short-range vs long-range	Rank-sum	114 (3)	84 (3)	Pairs	0.0347
Figure 7F	Short-range vs no change	T-test	114 (3)	-	Pairs	0.7058
	Long-range vs no change	T-test	84 (3)	-	Pairs	0.0435
	Short-range vs long-range	Rank-sum	114 (3)	84 (3)	Pairs	0.0199
Figure 7I	Short-range vs no change	T-test	114 (3)	-	Pairs	0.4865
	Long-range vs no change	T-test	84 (3)	-	Pairs	0.2184
	Short-range vs long-range	Rank-sum	114 (3)	84 (3)	Pairs	0.1633
Figure S4	C57BL/6					
	Closed loop vs no change	T-test	24 (4)	-	Regions	0.0277
	Open loop vs no change	T-test	24 (4)	-	Regions	0.6384
	Dark vs no change	T-test	24 (4)	-	Regions	$<10^{-4}$
	Tlx3					
	Closed loop vs no change	T-test	30 (5)	-	Regions	0.0365
	Open loop vs no change	T-test	30 (5)	-	Regions	0.0004
	Dark vs no change	T-test	30 (5)	-	Regions	0.0104
Figure S6E	Short-range vs no change	T-test	137 (4)	-	Pairs	0.0262
	Long-range vs no change	T-test	127 (4)	-	Pairs	0.0019
	Short-range vs long-range	Rank-sum	137 (4)	127 (4)	Pairs	0.9537

661

662

663 **Table S2. Indicator expression strategy in individual mice.**

Nbr. mice	Genotype	Virus	Figures
3	C57BL/6	AAV-PHP.eB-hSyn1-jGCaMP7f	**1C, 1F-1H, 1L, 2A and 2B, 3A-3C, 4A-4C, 5A and 5B, 6A-6C, S2, S3F, S4 and S5**
3	C57BL/6	AAV-PHP.eB-EF1α-GCaMP6s	**1F-1H, 1L, 2B, 3B and 3C, 4A-4C, 5A and 5B, 6A-6C, S2, S3F, S4**
8	C57BL/6	AAV-PHP.eB-EF1α-GFP	**S1**
4	Emx1-Cre	AAV-PHP.eB-DIO-EF1α-GCaMP6s	**1L and S3A**
4	Cux2-CreERT2 x Ai148	-	**1L, S3B and S6**
7	Scnn1a-Cre x Ai148	-	**1L and S3C**
15	Tlx3-Cre x Ai148	-	**1D, 1I-1L, 2C and 2D, 3D-3F, 4D-4F, 5C and 5D, 6D-6F, 7, 8, S2, S3D and S4**
3	Ntsr1-Cre x Ai148	-	**1L and S3E**
2	PV-Cre x Ai148	-	**1L and S3G**
6	VIP-Cre x Ai148	-	**1L and S3H**
4	SST-Cre	AAV-PHP.eB-DIO-EF1α-jGCaMP7f	**1L and S3I**
1	SST-Cre x Ai148	-	**1L and S3I**

664

METHODS

Key Resource Table

REAGENT or RESOURCE	Source	Identifier
Bacterial and virus strains		
AAV-PHP.eb-hSyn1-jGCaMP7f (10^{13} GC/ml)	FMI vector core	vector.fmi.ch
AAV-PHP.eb-EF1α-GCaMP6s (10^{13} GC/ml)	FMI vector core	vector.fmi.ch
AAV-PHP.eb-DIO-EF1α-GCaMP6s (10^{13} GC/ml)	FMI vector core	vector.fmi.ch
AAV-PHP.eb-DIO-EF1α-jGCaMP7f (10^{12} GC/ml)	FMI vector core	vector.fmi.ch
AAV-PHP.eb-EF1α-GFP (10^{13} GC/ml)	FMI vector core	vector.fmi.ch
Chemicals, peptides, and recombinant proteins		
Fentanyl citrate	Actavis	CAS 990-73-8
Midazolam (Dormicum)	Roche	CAS 59467-96-8
Medetomidine (Domitor)	Orion Pharma	CAS 86347-14-0
Ropivacaine	Presenius Kabi	CAS 132112-35-7
Lidocaine	Bichsel	CAS 137-58-6
Buprenorphine	Reckitt Benckiser Healthcare	CAS 52485-79-7
Ophthalmic gel (Humigel)	Virbac	N/A
Flumazenil (Anexate)	Roche	CAS 78755-81-4
Atipamezole (Antisedan)	Orion Pharma	CAS 104054-27-5
N-Butyl-2-cyanoacrylate (Histoacryl)	Braun	CAS 6606-65-1
Dental cement (Paladur)	Heraeus Kulzer	CAS 9066-86-8
Metacam	Boehringer Ingelheim	CAS 71125-39-8
Clozapine (powder)	Novartis	CAS 5786-21-0
Aripiprazole (intramuscular injection solution 7.5 mg/ml)	Otsuka Pharmaceutical	CAS 129722-12-9
Haloperidol (intramuscular injection solution 5 mg/ml)	Janssen	CAS 52-86-8
Amphetamine (powder)	Hänseler	CAS 60-13-9
Tamoxifen food	Envigo	CAS 10540-29-1 (TD.55125)
Deposited data		
All data and code used to generate manuscript figures	This paper	data.fmi.ch
Experimental models: Organisms/strains		
Mus musculus: C57BL/6	Charles River	N/A
Mus musculus: Emx1$^{tm1(cre)Krj}$	Jackson Laboratories	RRID: IMSR_JAX:005628
Mus musculus: B6(Cg)-Cux2$^{tm3.1(cre/ERT2)Mull}$/Mmmh	MMRRC	RRID:MMRRC_032779-MU
Mus musculus: Scnn1a-cre3Aibs/J	Jackson Laboratories	RRID:IMSR_JAX:009613
Mus musculus: Tg(Tlx3-cre)PL56Gsat/Mmucd	MMRRC	RRID:MMRRC_041158-UCD
Mus musculus: Ntsr1$^{GN220Gsat/Mmucd}$	MMRRC	RRID:MMRRC_017266-UCD
Mus musculus: Pvalb$^{tm1(cre)Arbr}$	Jackson Laboratories	RRID:IMSR_JAX:008069
Mus musculus: Vip$^{tm1(cre)Zjh}$	Jackson Laboratories	RRID:IMSR_JAX:010908
Mus musculus: Sst$^{tm2.1(cre)Zjh}$	Jackson Laboratories	RRID:IMSR_JAX:018973
Mus musculus: Igs7$^{tm148.1(tetO-GCaMP6f,CAG-tTA2)Hze}$/J	Jackson Laboratories	RRID:IMSR_JAX:030328
Software and algorithms		
MATLAB (2021a)	The MathWorks	RRID: SCR_001622
LabVIEW	National Instruments	RRID: SCR_014325
Python	python.org	RRID: SCR_008394
Panda3D	panda3d.org	N/A

Mice. All animal procedures were approved by and carried out in accordance with guidelines of the Veterinary Department of the Canton Basel-Stadt, Switzerland. The mice used for widefield imaging in this study were kept on a C57BL/6 background and were of the following genotype: 6 C57BL/6 (Charles River Laboratories), 4 Emx1-Cre (Gorski et al., 2002), 4 Cux2-CreERT2 (Franco et al., 2012), 7 Scnn1a-Cre (Madisen et al., 2010), 15 Tlx3-Cre (Gerfen et al., 2013), 3 Ntsr1-Cre (Gong et al., 2007), 2 PV-Cre (Hippenmeyer et al., 2005), 6 VIP-Cre (Taniguchi et al., 2011), and 5 SST-Cre (Taniguchi et al., 2011) mice. Ai148 ((Daigle et al., 2018), Jackson Laboratories, stock #030328) mice were used as breeders to drive GCaMP6f expression in Cre positive neurons. 8 C57BL/6 mice were used in experiments controlling for hemodynamic responses. To induce expression of Cre in the Cux2-CreERT2 line, mice were provided for at least 1 week with tamoxifen containing food (Envigo, 400 mg tamoxifen per kg of food) as their sole food source. Mice were group housed in a vivarium (light/dark cycle: 12/12 hours). Experimental mice were of either sex.

Surgery and virus injections. For all surgical procedures, mice were anesthetized using a mixture of fentanyl (0.05 mg/kg; Actavis), midazolam (5.0 mg/kg; Dormicum, Roche), and medetomidine (0.5 mg/kg; Domitor, Orion). In a subset of mice (6 C57BL/6, 4 Emx1-Cre, and 4 SST-Cre mice), we injected an AAV vector based on the PHP.eB capsid (Chan et al., 2017) retroorbitally (6 µl each eye of at least 10^{13} GC/ml) to drive expression of GCaMP under either the EF1α or hSyn1 promoter pan-neuronally, or in a cell type specific manner using a double-floxed inverted open reading frame (DIO) construct. For hemodynamic response control experiments (**Figure S1**), we used an AAV-PHP.eb-EF1α-GFP to pan-neuronally express GFP. To improve optical access to the cortex, we implanted crystal skull cranial windows (Kim et al., 2016). Prior to removing the skull plate overlying dorsal cortex, we recorded the location of bregma relative to other landmarks on the skull. Superglue (Pattex) was used to glue the crystal skull in place in the craniotomy. In a subset of mice, for the comparison of hemodynamic responses (**Figure S1**), we used a clear skull preparation (Guo et al., 2014). To do this, we attached the crystal skull coverslip directly onto the cleaned skull surface with a three-component polymer (C&B Metabond, Parkell). A custom-machined titanium head bar was attached to the skull using dental cement (Paladur, Heraeus). An epifluorescence overview image was taken to mark reference points on the dorsal cortical surface. Anesthesia was antagonized by an intraperitoneal injection of a mixture of flumazenil (0.5 mg/kg; Anexate, Roche) and atipamezole (2.5 mg/kg; Antisedan, Orion Pharma). For peri- and post-operative analgesia we injected buprenorphine (0.1 mg/kg; Reckitt Benckiser Healthcare (UK) Ltd.) and Metacam (5 mg/kg; Boehringer Ingelheim). Imaging commenced at the earliest 1 week after head bar implantation or 3 weeks after retroorbital AAV injection. Clozapine (Novartis), aripiprazole (Otsuka Pharmaceutical),

haloperidol (Janssen), or amphetamine (Hänseler) was intraperitoneally injected at 0.2 μg/g, 0.2 μg/g, 0.1 μg/g or 4 μg/g body weight, respectively.

Virtual reality setup and stimulus design. For all experiments we used a virtual reality setup as previously described (Leinweber et al., 2014). Mice were head-fixed and free to run on a spherical, air-supported Styrofoam ball. A virtual corridor was projected (using a Samsung SP-F10M projector) onto a toroidal screen positioned in front of the mouse covering a field of view of approximately 240 degrees horizontally and 100 degrees vertically. Recordings were blocked into 5-minute sessions. Experiments typically commenced with 4 sessions of a closed loop condition in which the rotation of the spherical treadmill was coupled to the movement in a virtual corridor. To introduce mismatches, we broke the coupling between locomotion and visual flow by briefly halting visual flow for 1 s at random times. Closed loop sessions were followed by 4 sessions of an open loop condition, in which rotation of the spherical treadmill and movement in the virtual corridor were decoupled. The visual stimulus consisted of a replay of the visual flow recorded in the previous closed loop condition. Following this we recorded 2 sessions of what we refer to as a dark condition in which the virtual reality was switched off. Please note, this was not complete darkness, primarily because the shielding of the blue excitation light was not light proof. Finally, we recorded activity in 2 sessions of a grating condition in which we presented drifting grating stimuli (8 directions of 6 s ± 2 s (mean ± SD) duration each with an inter-grating interval of 4.5 s ± 1.5 s (mean ± SD) gray screen, presented in randomized order). These sessions, totaling approximately 1 hour of recording time per day, were acquired for 3 consecutive days. For mice in which we went on to test the effect of drugs on dorsal cortex activity, the first post-drug injection data were acquired +1 h after drug injection (+30 mins in the case of amphetamine because of faster onset kinetics of the drug) and further data were collected at the +24 h and +48 h timepoints. Data in the manuscript are shown as the combined data over either all data collected before drug injection (labelled as naive) or after drug injection (labelled as clozapine, aripiprazole, haloperidol or amphetamine, respectively).

Data acquisition. All widefield imaging experiments were performed on a custom-built macroscope consisting of commercially available objectives mounted face-to-face (Nikon 85 mm/f1.8 sample side, Nikon 50 mm/f1.4 sensor side). We used a 470 nm LED (Thorlabs) powered by a custom-built LED driver for exciting GCaMP (or GFP) fluorescence through an excitation filter (SP490, Thorlabs) reflected off a dichroic mirror (LP490, Thorlabs) placed in the parfocal plane of the objectives. Green fluorescence was collected through a 525/50 emission filter on an sCMOS camera (PCO edge 4.2). Apertures on objectives were usually kept maximally open and the current at the LED driver was used to adjust fluorescence intensity to a value that was kept below 25% of the maximum dynamic

range of the sensor. In cases where this was not possible (e.g., transfection of GFP yielded extremely bright fluorescence, often visible with the naked eye), objective apertures were gradually reduced to avoid overexposure of the sensor. LED illumination was adjusted with a collimator (Thorlabs SM2F32-A) to achieve homogenous illumination across the surface of the cranial window. The resulting gaussian profile of the illumination cone was further trimmed with black tape on the sample side objective to avoid light shining directly into the mouse's eye. An Arduino board (Arduino Mega 2560) was used to control LED onsets synced to the frame trigger signal of the camera. The duty cycle of the 470 nm LED was 90%. Raw images were acquired at full speed (100 Hz; except for GFP controls, which were acquired at 50 Hz effective frame rate) and full dynamic range (16 bit) of the sensor. The raw images were cropped on-sensor and the resulting data was streamed to disk with custom written software in LabVIEW (National Instruments), resulting in an effective pixel size of 6 μm^2 at a standardized imaging resolution of 1108 pixels x 1220 pixels (1.35 MP).

Data processing. Off-line data processing and data analysis (section below) were done with custom-written MATLAB (2021a) scripts. Raw movie data was manually registered across days by aligning subsequent mean projections of the data to the first recorded image sequence. We placed regions of interest (ROIs) relative to readily identifiable anatomical landmarks that had been previously noted during cranial window surgery (see above). This resulted in the selection of six 20 pixels x 20 pixels ROIs per hemisphere. Of those ROIs, we calculated the activity as the $\Delta F/F_0$, wherein F_0 was the median fluorescence of the recording (approximately 30 000 frames in a 5 min recording). $\Delta F/F_0$ was corrected for slow fluorescence drift caused by thermal brightening of the LED using 8^{th} percentile filtering with a 62.5 s moving window similar to what was described previously for two-photon imaging (Dombeck et al., 2007).

Data analysis. Locomotion and visual flow onsets were determined based on threshold crossing of locomotion or visual flow speed. To select only well isolated onsets, we used a speed threshold of 30 cm/s and excluded all onsets with locomotion or visual flow in the 3 s window preceding the onset. To increase the number of locomotion onsets that passed the speed threshold criterion for the GFP imaging data (**Figure S1**), we excluded only those onsets if there was locomotion in the 1 s window preceding onset.

All stimulus response curves (**Figures 1F-1L, 3B and 3C, 3E and 3F, 4, 8, S1-S3**) were baseline subtracted. The baseline subtraction window for unpredictable stimuli (mismatch and grating) was -200 ms to 0 ms before stimulus onset. For closed loop and open loop locomotion onsets, and open loop visual flow onsets, to accommodate calcium indicator offset dynamics and potential

anticipatory activity, we placed the baseline subtraction windows for these onsets at -2900 ms to -2700 ms for GCaMP imaging, or -900 ms to -700 ms for GFP imaging. Varying this window within the bounds of offset dynamics of the indicator and anticipatory activity onset did not change the conclusions drawn in this manuscript. Analyses in which image sequences were aligned to event onsets (**Figures 1C-1D and 3**) used the same parameters as above.

On rare occasions, we observed seizure-like activity after antipsychotic drug injection. These events resulted in atypically high levels of correlation, and to avoid them from influencing our conclusions we excluded these data from further analysis. We excluded sessions if they contained an event in which average activity of all 12 ROIs remained elevated above 30% $\Delta F/F$ for more than 10 s. This criterion led to the exclusion of 0.26% of data (10 out of 3801 of 5 min recording sessions).

To quantify the similarity of closed loop and open loop locomotion onset responses shown in **Figure 1L** we calculated the correlation coefficient between the averaged responses (onsets and mice, 1 s moving average) in a window -5 s to +3 s, for each ROI.

To calculate the maps that show the timing of activation of individual dorsal cortex regions (**Figures 3B and 3C, 3E and 3F**), we first aligned the craniotomies of all mice within one genotype to the first mouse's average grating response map and then calculated an average dorsal cortex response time course. For each pixel of this image sequence, we then determined the time at which the pixel's value crossed a threshold of the maximum value in the entire time course, divided by 6 standard deviations of the pixel's baseline value (-200 ms to 0 ms before event onset, as stated above). The resulting maps were denoised using a Gaussian filter and we removed all pixel clusters that contained fewer than 500 connected pixels. For illustration purposes, these maps were overlaid over an example crystal skull craniotomy to produce the panels shown in **Figure 3**.

For the correlation analyses shown in **Figures 5-7, S5 and S6**, we first calculated the correlation coefficient of neuronal activity for all possible pairs of the 12 regions of interest. We then determined the distance between each pair of ROIs and normalized this value by the distance between bregma and lambda obtained from the images during initial surgery for each mouse (**Figure S5A**). We plotted the correlation against the distance for each pair of regions of interest and binned the data in a 40 x 40 grid and smoothed the resulting image with a gaussian filter (**Figure S5B**), to obtain the heatmaps shown in **Figures 6A and 6B, 6D and 6E, 7A and 7B, 7D and 7E, 7G and 7H, S5B, S6C and S6D**. Contour lines in the heatmaps were then drawn to 50% of the maximum value in the plot. The boxplot quantifications (**Figures 6C, 6F, 7C, 7F, 7I, S6E**) were calculated as the change in correlation coefficient of activity after and before treatment for all pairs of regions of interest,

normalized to the value before treatment and split into short- and long-range using a threshold of 0.9 of the bregma-lambda distance for each mouse.

For **Figure S2,** onset aligned data were first averaged for each mouse and then summed in the given combinations. The SEM was calculated over mice. For visualization purposes, we omitted the SEM from the open loop locomotion and open loop visual flow onset traces.

To obtain the differences in the correlation between activity and locomotion after and before clozapine injection (**Figure S4**), we first averaged all correlation coefficients in the individual sessions of a condition (closed loop, open loop, or dark) to generate one correlation coefficient per mouse and ROI, for each condition. We then calculated and plotted the difference between these correlation values after and before clozapine injection.

ACKNOWLEDGEMENTS

We thank Tingjia Lu for production of the AAV vectors, Rebecca Jordan for performing the clear skull implants used in the hemodynamic response measurements, and members of the Keller lab for discussion and support. This project has received funding from the Swiss National Science Foundation, the Novartis Research Foundation, and the European Research Council (ERC) under the European Union's Horizon 2020 research and innovation programme (grant agreement No 865617).

AUTHOR CONTRIBUTIONS

MH performed the experiments and analyzed the data. All authors wrote the manuscript.

CONFLICT OF INTEREST

Part of the results presented herein have been included in patent application EP22153051.1.

818 **REFERENCES**

819 Allen, W.E., Kauvar, I.V., Chen, M.Z., Richman, E.B., Yang, S.J., Chan, K., Gradinaru, V., Deverman,
820 B.E., Luo, L., and Deisseroth, K. (2017). Global Representations of Goal-Directed Behavior in Distinct
821 Cell Types of Mouse Neocortex. Neuron *94*, 891-907.e6.

822 Anderson, C.T., Sheets, P.L., Kiritani, T., and Shepherd, G.M.G. (2010). Sublayer-specific microcircuits
823 of corticospinal and corticostriatal neurons in motor cortex. Nat Neurosci *13*, 739–744.

824 Aravanis, A.M., Wang, L.-P., Zhang, F., Meltzer, L.A., Mogri, M.Z., Schneider, M.B., and Deisseroth, K.
825 (2007). An optical neural interface: in vivo control of rodent motor cortex with integrated fiberoptic
826 and optogenetic technology. J Neural Eng *4*, S143-156.

827 Attinger, A., Wang, B., and Keller, G.B. (2017). Visuomotor Coupling Shapes the Functional
828 Development of Mouse Visual Cortex. Cell *169*, 1291-1302.e14.

829 Audette, N.J., Zhou, W., and Schneider, D.M. (2021). Temporally precise movement-based
830 predictions in the mouse auditory cortex.

831 Ayaz, A., Stäuble, A., Hamada, M., Wulf, M.A., Saleem, A.B., and Helmchen, F. (2019). Layer-specific
832 integration of locomotion and sensory information in mouse barrel cortex. Nature Communications
833 *10*, 1–14.

834 Bastos, A.M., Usrey, W.M., Adams, R.A., Mangun, G.R., Fries, P., and Friston, K.J. (2012). Canonical
835 microcircuits for predictive coding. Neuron *76*, 695–711.

836 Catafau, A.M., Parellada, E., Lomeña, F.J., Bernardo, M., Pavía, J., Ros, D., Setoain, J., and Gonzalez-
837 Monclús, E. (1994). Prefrontal and temporal blood flow in schizophrenia: resting and activation
838 technetium-99m-HMPAO SPECT patterns in young neuroleptic-naive patients with acute disease. J
839 Nucl Med *35*, 935–941.

840 Chan, K.Y., Jang, M.J., Yoo, B.B., Greenbaum, A., Ravi, N., Wu, W.-L., Sánchez-Guardado, L., Lois, C.,
841 Mazmanian, S.K., Deverman, B.E., et al. (2017). Engineered AAVs for efficient noninvasive gene
842 delivery to the central and peripheral nervous systems. Nat Neurosci *20*, 1172–1179.

843 Constantinople, C.M., and Bruno, R.M. (2013). Deep cortical layers are activated directly by
844 thalamus. Science (New York, N.Y.) *340*, 1591–1594.

845 Daigle, T.L., Madisen, L., Hage, T.A., Valley, M.T., Knoblich, U., Larsen, R.S., Takeno, M.M., Huang, L.,
846 Gu, H., Larsen, R., et al. (2018). A Suite of Transgenic Driver and Reporter Mouse Lines with
847 Enhanced Brain-Cell-Type Targeting and Functionality. Cell *174*, 465-480.e22.

848 Dierks, T., Linden, D.E., Jandl, M., Formisano, E., Goebel, R., Lanfermann, H., and Singer, W. (1999).
849 Activation of Heschl's gyrus during auditory hallucinations. Neuron *22*, 615–621.

850 Dombeck, D.A., Khabbaz, A.N., Collman, F., Adelman, T.L., and Tank, D.W. (2007). Imaging large-scale
851 neural activity with cellular resolution in awake, mobile mice. Neuron *56*, 43–57.

852 Douglas, R.J., and Martin, K.A. (1991). A functional microcircuit for cat visual cortex. The Journal of
853 Physiology *440*, 735–769.

Eliades, S.J., and Wang, X. (2008). Neural substrates of vocalization feedback monitoring in primate auditory cortex. Nature *453*, 1102–1106.

Fletcher, P.C., and Frith, C.D. (2009). Perceiving is believing: a Bayesian approach to explaining the positive symptoms of schizophrenia. Nature Reviews. Neuroscience *10*, 48–58.

Franco, S.J., Gil-Sanz, C., Martinez-Garay, I., Espinosa, A., Harkins-Perry, S.R., Ramos, C., and Müller, U. (2012). Fate-Restricted Neural Progenitors in the Mammalian Cerebral Cortex. Science.

Frith, C. (2005). The neural basis of hallucinations and delusions. Comptes Rendus Biologies *328*, 169–175.

Garner, A.R., and Keller, G.B. (2022). A cortical circuit for audio-visual predictions. Nat Neurosci *25*, 98–105.

Gerfen, C.R., Paletzki, R., and Heintz, N. (2013). GENSAT BAC Cre-Recombinase Driver Lines to Study the Functional Organization of Cerebral Cortical and Basal Ganglia Circuits. Neuron *80*, 1368–1383.

Gong, S., Doughty, M., Harbaugh, C.R., Cummins, A., Hatten, M.E., Heintz, N., and Gerfen, C.R. (2007). Targeting Cre Recombinase to Specific Neuron Populations with Bacterial Artificial Chromosome Constructs. J. Neurosci. *27*, 9817–9823.

Gorski, J.A., Talley, T., Qiu, M., Puelles, L., Rubenstein, J.L.R., and Jones, K.R. (2002). Cortical excitatory neurons and glia, but not GABAergic neurons, are produced in the Emx1-expressing lineage. J Neurosci *22*, 6309–6314.

Guo, Z.V., Li, N., Huber, D., Ophir, E., Gutnisky, D., Ting, J.T., Feng, G., and Svoboda, K. (2014). Flow of cortical activity underlying a tactile decision in mice. Neuron *81*, 179–194.

Haarsma, J., Kok, P., and Browning, M. (2020). The promise of layer-specific neuroimaging for testing predictive coding theories of psychosis. Schizophrenia Research.

Harrison, P.J., and Weinberger, D.R. (2005). Schizophrenia genes, gene expression, and neuropathology: on the matter of their convergence. Mol Psychiatry *10*, 40–68.

Heindorf, M., Arber, S., and Keller, G.B. (2018). Mouse Motor Cortex Coordinates the Behavioral Response to Unpredicted Sensory Feedback. Neuron *99*, 1040-1054.e5.

Hippenmeyer, S., Vrieseling, E., Sigrist, M., Portmann, T., Laengle, C., Ladle, D.R., and Arber, S. (2005). A Developmental Switch in the Response of DRG Neurons to ETS Transcription Factor Signaling. PLOS Biology *3*, e159.

Javitt, D.C. (2009). Sensory Processing in Schizophrenia: Neither Simple nor Intact. Schizophr Bull *35*, 1059–1064.

Jiang, L.P., and Rao, R.P.N. (2021). Predictive Coding Theories of Cortical Function. ArXiv:2112.10048 [q-Bio].

Jordan, M.I., and Rumelhart, D.E. (1992). Forward Models: Supervised Learning with a Distal Teacher. Cognitive Science *16*, 307–354.

889 Jordan, R., and Keller, G.B. (2020). Opposing Influence of Top-down and Bottom-up Input on
890 Excitatory Layer 2/3 Neurons in Mouse Primary Visual Cortex. Neuron *108*, 1194-1206.e5.

891 Keller, G.B., and Hahnloser, R.H.R. (2009). Neural processing of auditory feedback during vocal
892 practice in a songbird. Nature *457*, 187–190.

893 Keller, G.B., and Mrsic-Flogel, T.D. (2018). Predictive Processing: A Canonical Cortical Computation.
894 Neuron *100*, 424–435.

895 Keller, G.B., Bonhoeffer, T., and Hübener, M. (2012). Sensorimotor mismatch signals in primary
896 visual cortex of the behaving mouse. Neuron *74*, 809–815.

897 Kim, T.H., Zhang, Y., Lecoq, J., Jung, J.C., Li, J., Zeng, H., Niell, C.M., and Schnitzer, M.J. (2016). Long-
898 Term Optical Access to an Estimated One Million Neurons in the Live Mouse Cortex. Cell Rep *17*,
899 3385–3394.

900 Kiritani, T., Wickersham, I.R., Seung, H.S., and Shepherd, G.M.G. (2012). Hierarchical connectivity and
901 connection-specific dynamics in the corticospinal-corticostriatal microcircuit in mouse motor cortex.
902 J Neurosci *32*, 4992–5001.

903 Le Bihan, D., Turner, R., Zeffiro, T.A., Cuénod, C.A., Jezzard, P., and Bonnerot, V. (1993). Activation of
904 human primary visual cortex during visual recall: a magnetic resonance imaging study. Proceedings
905 of the National Academy of Sciences of the United States of America *90*, 11802–11805.

906 Leinweber, M., Zmarz, P., Buchmann, P., Argast, P., Hübener, M., Bonhoeffer, T., and Keller, G.B.
907 (2014). Two-photon calcium imaging in mice navigating a virtual reality environment. Journal of
908 Visualized Experiments : JoVE e50885.

909 Leinweber, M., Ward, D.R., Sobczak, J.M., Attinger, A., and Keller, G.B. (2017). A Sensorimotor Circuit
910 in Mouse Cortex for Visual Flow Predictions. Neuron *95*, 1420-1432.e5.

911 Li, S., Hu, N., Zhang, W., Tao, B., Dai, J., Gong, Y., Tan, Y., Cai, D., and Lui, S. (2019). Dysconnectivity of
912 Multiple Brain Networks in Schizophrenia: A Meta-Analysis of Resting-State Functional Connectivity.
913 Front. Psychiatry *0*.

914 Li, T., Wang, Q., Zhang, J., Rolls, E.T., Yang, W., Palaniyappan, L., Zhang, L., Cheng, W., Yao, Y., Liu, Z.,
915 et al. (2017). Brain-Wide Analysis of Functional Connectivity in First-Episode and Chronic Stages of
916 Schizophrenia. Schizophr Bull *43*, 436–448.

917 Ma, Y., Shaik, M.A., Kim, S.H., Kozberg, M.G., Thibodeaux, D.N., Zhao, H.T., Yu, H., and Hillman,
918 E.M.C. (2016). Wide-field optical mapping of neural activity and brain haemodynamics:
919 considerations and novel approaches. Philosophical Transactions of the Royal Society B: Biological
920 Sciences *371*, 20150360.

921 Madisen, L., Zwingman, T.A., Sunkin, S.M., Oh, S.W., Zariwala, H.A., Gu, H., Ng, L.L., Palmiter, R.D.,
922 Hawrylycz, M.J., Jones, A.R., et al. (2010). A robust and high-throughput Cre reporting and
923 characterization system for the whole mouse brain. Nature Neuroscience *13*, 133–140.

924 Maia, T.V., and Frank, M.J. (2017). An Integrative Perspective on the Role of Dopamine in
925 Schizophrenia. Biol Psychiatry *81*, 52–66.

926 Moghaddam, B., and Javitt, D. (2012). From Revolution to Evolution: The Glutamate Hypothesis of
927 Schizophrenia and its Implication for Treatment. Neuropsychopharmacol *37*, 4–15.

928 Morita, K., Im, S., and Kawaguchi, Y. (2019). Differential Striatal Axonal Arborizations of the
929 Intratelencephalic and Pyramidal-Tract Neurons: Analysis of the Data in the MouseLight Database.
930 Frontiers in Neural Circuits *13*.

931 Musall, S., Kaufman, M.T., Juavinett, A.L., Gluf, S., and Churchland, A.K. (2019). Single-trial neural
932 dynamics are dominated by richly varied movements. Nat Neurosci *22*, 1677–1686.

933 Northoff, G., and Duncan, N.W. (2016). How do abnormalities in the brain's spontaneous activity
934 translate into symptoms in schizophrenia? From an overview of resting state activity findings to a
935 proposed spatiotemporal psychopathology. Prog Neurobiol *145–146*, 26–45.

936 Oberlaender, M., Ramirez, A., and Bruno, R.M. (2012). Sensory Experience Restructures
937 Thalamocortical Axons during Adulthood. Neuron *74*, 648–655.

938 Pakan, J.M., Lowe, S.C., Dylda, E., Keemink, S.W., Currie, S.P., Coutts, C.A., and Rochefort, N.L.
939 (2016). Behavioral-state modulation of inhibition is context-dependent and cell type specific in
940 mouse visual cortex. ELife *5*.

941 Parellada, M., Gomez-Vallejo, S., Burdeus, M., and Arango, C. (2017). Developmental Differences
942 Between Schizophrenia and Bipolar Disorder. Schizophr Bull *43*, 1176–1189.

943 Rao, R.P.N., and Ballard, D.H. (1999). Predictive coding in the visual cortex: a functional
944 interpretation of some extra-classical receptive-field effects. Nature Neuroscience *2*, 79–87.

945 Saleem, A.B., Ayaz, A., Jeffery, K.J., Harris, K.D., and Carandini, M. (2013). Integration of visual
946 motion and locomotion in mouse visual cortex. Nature Neuroscience *16*, 1864–1869.

947 Schmack, K., Bosc, M., Ott, T., Sturgill, J.F., and Kepecs, A. (2021). Striatal dopamine mediates
948 hallucination-like perception in mice. Science *372*, eabf4740.

949 Shergill, S.S., Brammer, M.J., Williams, S.C., Murray, R.M., and McGuire, P.K. (2000). Mapping
950 auditory hallucinations in schizophrenia using functional magnetic resonance imaging. Arch Gen
951 Psychiatry *57*, 1033–1038.

952 Singh, T., Neale, B.M., Daly, M.J., and Consortium, on behalf of the S.E.M.-A. (SCHEMA) (2020).
953 Exome sequencing identifies rare coding variants in 10 genes which confer substantial risk for
954 schizophrenia.

955 Stanley, J., and Miall, R.C. (2007). Functional activation in parieto-premotor and visual areas
956 dependent on congruency between hand movement and visual stimuli during motor-visual priming.
957 NeuroImage *34*, 290–299.

958 Stringer, C., Pachitariu, M., Steinmetz, N., Reddy, C.B., Carandini, M., and Harris, K.D. (2019).
959 Spontaneous behaviors drive multidimensional, brainwide activity. Science *364*, 255.

960 Suzuki, M., and Larkum, M.E. (2020). General Anesthesia Decouples Cortical Pyramidal Neurons. Cell
961 *180*, 666-676.e13.

962 Taniguchi, H., He, M., Wu, P., Kim, S., Paik, R., Sugino, K., Kvitsani, D., Fu, Y., Lu, J., Lin, Y., et al.
963 (2011). A Resource of Cre Driver Lines for Genetic Targeting of GABAergic Neurons in Cerebral
964 Cortex. Neuron *71*, 995–1013.

965 Valley, M.T., Moore, M.G., Zhuang, J., Mesa, N., Castelli, D., Sullivan, D., Reimers, M., and Waters, J.
966 (2020). Separation of hemodynamic signals from GCaMP fluorescence measured with wide-field
967 imaging. J Neurophysiol *123*, 356–366.

968 Wekselblatt, J.B., Flister, E.D., Piscopo, D.M., and Niell, C.M. (2016). Large-scale imaging of cortical
969 dynamics during sensory perception and behavior. Journal of Neurophysiology *115*, 2852–2866.

970 Widmer, F.C., and Keller, G.B. (2021). Developmental plasticity in visual cortex is necessary for
971 normal visuomotor integration and visuomotor skill learning. BioRxiv 2021.06.20.449148.

972 Xu, X., Olivas, N.D., Ikrar, T., Peng, T., Holmes, T.C., Nie, Q., and Shi, Y. (2016). Primary visual cortex
973 shows laminar-specific and balanced circuit organization of excitatory and inhibitory synaptic
974 connectivity. The Journal of Physiology *594*, 1891–1910.

975 Yamawaki, N., and Shepherd, G.M.G. (2015). Synaptic circuit organization of motor corticothalamic
976 neurons. J Neurosci *35*, 2293–2307.

977 Yoon, J.H., Rokem, A.S., Silver, M.A., Minzenberg, M.J., Ursu, S., Ragland, J.D., and Carter, C.S. (2009).
978 Diminished orientation-specific surround suppression of visual processing in schizophrenia.
979 Schizophr Bull *35*, 1078–1084.

980 Zmarz, P., and Keller, G.B. (2016). Mismatch Receptive Fields in Mouse Visual Cortex. Neuron *92*,
981 766–772.

982